journal of the international meteor organization

WGN

44:6
december 2016

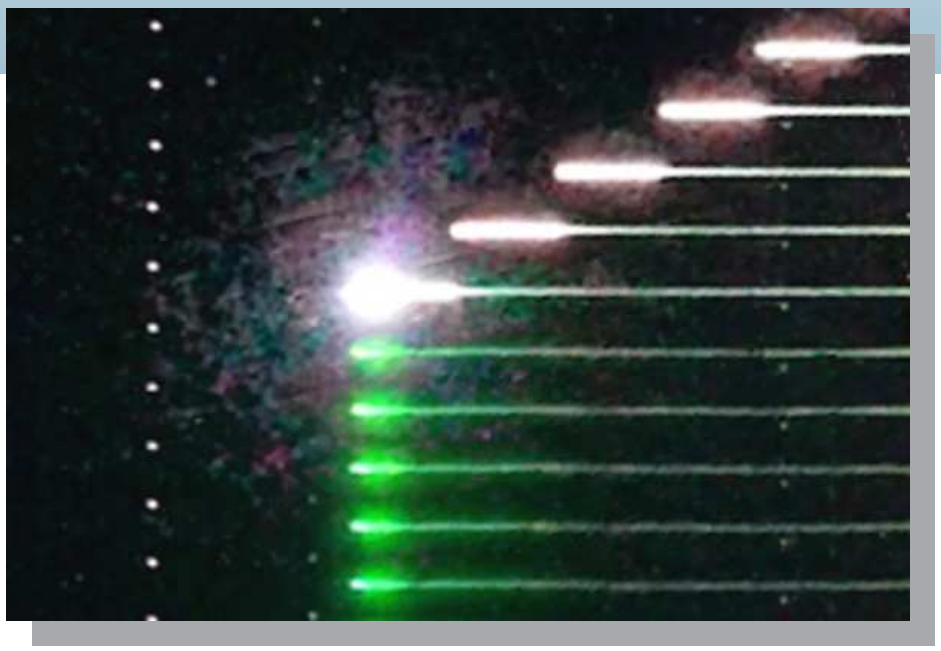

Solar longitudes for 2017
Detailed announcement of IMC 2017 in Petnica
Delta Mensids confirmed by CAMS New Zealand
Film recording of meteors using digital film cameras
June–July video meteors

ISSN 1016-3115

WGN Vol. 44, No. 6, December 2016, pp. 179 – 210

Administrative

Editorial *Javor Kac* 179

Solar Longitudes for 2017 *Rainer Arlt* 179

Conferences

Thirty-Sixth International Meteor Conference, Petnica, Serbia, September 21–24, 2017 *Dušan Pavlović and Nikola Božić* 181

Meteor science

Confirmation of the delta Mensids (IAU#130, DME) *Peter Jenniskens, Jack Baggaley, Ian Crumpton, and Peter Aldous* 187

Meteor Film Recording with Digital Film Cameras with large CMOS Sensors *Peter C. Slansky* 190

Preliminary results

Results of the IMO Video Meteor Network — June 2016, and photometry algorithms *Sirko Molau, Stefano Crivello, Rui Goncalves, Carlos Saraiva, Enrico Stomeo, and Javor Kac* 198

Results of the IMO Video Meteor Network — July 2016 *Sirko Molau, Stefano Crivello, Rui Goncalves, Carlos Saraiva, Enrico Stomeo, and Javor Kac* 205

Front cover photo

Aurigid fireball recorded on 2014 September 1, $05^{h}44^{m}44^{s}$ UTC, from La Palma, Canary Island. The original film sequence was shot at 25 fps with a Sony α7S set at ISO 200 000 with a Zeiss ZE Sonnar 2.8/35 mm. See also page 190 for details. Photo courtesy: Peter C. Slansky.

Back over photo

Composite image of 45 Perseids filmed on 2016 August 12/13 from from Emberger Alm, Austria, shot with a Canon ME20F-SH with a Canon USM II 1.4/35 mm lens. The film was recorded with 25 fps, and ISO 1 400 000 at $F = 2.0$. Image courtesy: Peter C. Slansky.

Writing for WGN

This Journal welcomes papers submitted for publication. All papers are reviewed for scientific content, and edited for English and style. Instructions for authors can be found in WGN **31:4**, 124–128, and at `http://www.imo.net/docs/writingforwgn.pdf` .

Copyright

It is the aim of WGN to increase the spread of scientific information, not to restrict it. When material is submitted to WGN for publication, this is taken as indicating that the author(s) grant(s) permission for WGN and the IMO to publish this material any number of times, in any format(s), without payment. This permission is taken as covering rights to reproduce both the content of the material and its form and appearance, including images and typesetting. Formats include paper, CD-ROM and the world-wide web. Other than these conditions, all rights remain with the author(s).
When material is submitted for publication, this is also taken as indicating that the author(s) claim(s) the right to grant the permissions described above.

Legal address

International Meteor Organization, Jozef Mattheessensstraat 60, 2540 Hove, Belgium.

Editorial

Javor Kac

Another year is closing, and with it, the 44th volume of *WGN*. We are grateful to the authors that wrote and submitted the papers. I counted 59 individuals that authored or co-authored articles in 2016. Although I still handled about 80% of the papers that were published this year, I am indebted to David Asher, Jürgen Rendtel and Felix Bettonvil who were the other handling editors for this volume. Other members of the editorial board and some other individuals acted as reviewers, proofreaders and advisors, and contributed to the journal quality as well. As in all the years since I started as WGN Editor-in-Chief in 2008, I also took care for the LaTeX typesetting and producing the electronic version of the journal, thus basically acting as technical editor.

Similar to the past years, we only received a handful of meteor-related photographs this year that we could use for the front and back covers. If you think you have a suitable meteor-related photograph, please offer it to us. You can send your photographs to `wgn@imo.net`. Also, if you notice a great meteor-related photograph online, please encourage the author to contact us at the same address, or alert us about the photo.

Last but not least, let me wish you a successful meteor year in 2017, with great satisfaction under the skies. Do not forget to write about your observations and analyses in *WGN*!

IMO bibcode WGN-446-editorial NASA-ADS bibcode 2016JIMO...44..179K

Solar Longitudes for 2017

Compiled by Rainer Arlt

A conversion table of dates to solar longitudes using (Steyaert, 1991) is given as every year. The longitudes are given on the next page; they are only valid for 2017. The conversion formulae for any time of the day are repeated here for your convenience.

If you want to calculate the solar longitude $\lambda_\odot$ of a specific time of the day, you may use a linear interpolation between two dates. Suppose you have a certain *Date* and the *Time* in hours (UT), you get the solar longitude by

$$\lambda_\odot = \lambda_{\odot,\mathrm{Date}} + (\lambda_{\odot,\mathrm{NextDay}} - \lambda_{\odot,\mathrm{Date}}) \times \frac{\mathrm{Time}}{24\ ^\mathrm{h}}.$$

Alternatively, if you want to convert a certain solar longitude $\lambda_\odot$ into a time of the day, look up the *Date* with the next-smaller solar longitude in the table and calculate

$$\mathrm{Time} = \frac{(\lambda_\odot - \lambda_{\odot,\mathrm{Date}})}{(\lambda_{\odot,\mathrm{NextDay}} - \lambda_{\odot,\mathrm{Date}})} \times 24\ ^\mathrm{h}.$$

The solar longitudes of 1988–2020 are given in two-hour increments and with three decimals at `http://www.imo.net/resources/solar-longitude-tables/`.

References

Steyaert C. (1991). "Calculating the solar longitude 2000.0". *WGN, Journal of the IMO*, **19:2**, 31–34.

IMO bibcode WGN-446-arlt-solarlong
NASA-ADS bibcode 2016JIMO...44..179A

Solar longitudes 2017. Dates refer to 00^h UT.

Jan	1	280.52	Mar	1	340.36	May	1	40.58	Jul	1	99.13	Sep	1	158.52	Nov	1	218.52
Jan	2	281.54	Mar	2	341.36	May	2	41.55	Jul	2	100.08	Sep	2	159.49	Nov	2	219.52
Jan	3	282.56	Mar	3	342.36	May	3	42.52	Jul	3	101.04	Sep	3	160.45	Nov	3	220.52
Jan	4	283.58	Mar	4	343.37	May	4	43.49	Jul	4	101.99	Sep	4	161.42	Nov	4	221.52
Jan	5	284.60	Mar	5	344.37	May	5	44.46	Jul	5	102.94	Sep	5	162.39	Nov	5	222.52
Jan	6	285.62	Mar	6	345.37	May	6	45.43	Jul	6	103.90	Sep	6	163.36	Nov	6	223.52
Jan	7	286.64	Mar	7	346.37	May	7	46.40	Jul	7	104.85	Sep	7	164.33	Nov	7	224.52
Jan	8	287.66	Mar	8	347.37	May	8	47.37	Jul	8	105.80	Sep	8	165.30	Nov	8	225.53
Jan	9	288.68	Mar	9	348.37	May	9	48.33	Jul	9	106.75	Sep	9	166.27	Nov	9	226.53
Jan	10	289.70	Mar	10	349.37	May	10	49.30	Jul	10	107.71	Sep	10	167.24	Nov	10	227.54
Jan	11	290.72	Mar	11	350.37	May	11	50.27	Jul	11	108.66	Sep	11	168.21	Nov	11	228.54
Jan	12	291.73	Mar	12	351.37	May	12	51.23	Jul	12	109.61	Sep	12	169.19	Nov	12	229.55
Jan	13	292.75	Mar	13	352.36	May	13	52.20	Jul	13	110.57	Sep	13	170.16	Nov	13	230.55
Jan	14	293.77	Mar	14	353.36	May	14	53.16	Jul	14	111.52	Sep	14	171.13	Nov	14	231.56
Jan	15	294.79	Mar	15	354.36	May	15	54.12	Jul	15	112.47	Sep	15	172.11	Nov	15	232.57
Jan	16	295.81	Mar	16	355.35	May	16	55.09	Jul	16	113.43	Sep	16	173.08	Nov	16	233.57
Jan	17	296.83	Mar	17	356.35	May	17	56.05	Jul	17	114.38	Sep	17	174.06	Nov	17	234.58
Jan	18	297.84	Mar	18	357.34	May	18	57.02	Jul	18	115.34	Sep	18	175.03	Nov	18	235.59
Jan	19	298.86	Mar	19	358.34	May	19	57.98	Jul	19	116.29	Sep	19	176.01	Nov	19	236.60
Jan	20	299.88	Mar	20	359.33	May	20	58.94	Jul	20	117.25	Sep	20	176.99	Nov	20	237.61
Jan	21	300.90	Mar	21	0.33	May	21	59.90	Jul	21	118.20	Sep	21	177.97	Nov	21	238.62
Jan	22	301.91	Mar	22	1.32	May	22	60.87	Jul	22	119.15	Sep	22	178.94	Nov	22	239.63
Jan	23	302.93	Mar	23	2.31	May	23	61.83	Jul	23	120.11	Sep	23	179.92	Nov	23	240.64
Jan	24	303.95	Mar	24	3.30	May	24	62.79	Jul	24	121.07	Sep	24	180.90	Nov	24	241.65
Jan	25	304.97	Mar	25	4.30	May	25	63.75	Jul	25	122.02	Sep	25	181.88	Nov	25	242.66
Jan	26	305.98	Mar	26	5.29	May	26	64.71	Jul	26	122.98	Sep	26	182.86	Nov	26	243.67
Jan	27	307.00	Mar	27	6.28	May	27	65.67	Jul	27	123.93	Sep	27	183.84	Nov	27	244.69
Jan	28	308.02	Mar	28	7.27	May	28	66.63	Jul	28	124.89	Sep	28	184.82	Nov	28	245.70
Jan	29	309.03	Mar	29	8.26	May	29	67.59	Jul	29	125.84	Sep	29	185.81	Nov	29	246.71
Jan	30	310.05	Mar	30	9.25	May	30	68.55	Jul	30	126.80	Sep	30	186.79	Nov	30	247.72
Jan	31	311.06	Mar	31	10.23	May	31	69.51	Jul	31	127.76						
Feb	1	312.08	Apr	1	11.22	Jun	1	70.47	Aug	1	128.71	Oct	1	187.77	Dec	1	248.74
Feb	2	313.10	Apr	2	12.21	Jun	2	71.43	Aug	2	129.67	Oct	2	188.75	Dec	2	249.75
Feb	3	314.11	Apr	3	13.19	Jun	3	72.39	Aug	3	130.63	Oct	3	189.74	Dec	3	250.76
Feb	4	315.12	Apr	4	14.18	Jun	4	73.34	Aug	4	131.58	Oct	4	190.72	Dec	4	251.78
Feb	5	316.14	Apr	5	15.16	Jun	5	74.30	Aug	5	132.54	Oct	5	191.71	Dec	5	252.79
Feb	6	317.15	Apr	6	16.15	Jun	6	75.26	Aug	6	133.50	Oct	6	192.69	Dec	6	253.80
Feb	7	318.16	Apr	7	17.13	Jun	7	76.21	Aug	7	134.46	Oct	7	193.68	Dec	7	254.82
Feb	8	319.18	Apr	8	18.12	Jun	8	77.17	Aug	8	135.41	Oct	8	194.66	Dec	8	255.83
Feb	9	320.19	Apr	9	19.10	Jun	9	78.13	Aug	9	136.37	Oct	9	195.65	Dec	9	256.85
Feb	10	321.20	Apr	10	20.08	Jun	10	79.08	Aug	10	137.33	Oct	10	196.64	Dec	10	257.87
Feb	11	322.21	Apr	11	21.06	Jun	11	80.04	Aug	11	138.29	Oct	11	197.63	Dec	11	258.88
Feb	12	323.22	Apr	12	22.04	Jun	12	80.99	Aug	12	139.25	Oct	12	198.61	Dec	12	259.90
Feb	13	324.23	Apr	13	23.02	Jun	13	81.95	Aug	13	140.21	Oct	13	199.60	Dec	13	260.92
Feb	14	325.24	Apr	14	24.00	Jun	14	82.90	Aug	14	141.17	Oct	14	200.59	Dec	14	261.93
Feb	15	326.25	Apr	15	24.98	Jun	15	83.86	Aug	15	142.13	Oct	15	201.59	Dec	15	262.95
Feb	16	327.26	Apr	16	25.96	Jun	16	84.81	Aug	16	143.09	Oct	16	202.58	Dec	16	263.97
Feb	17	328.27	Apr	17	26.94	Jun	17	85.77	Aug	17	144.05	Oct	17	203.57	Dec	17	264.99
Feb	18	329.28	Apr	18	27.92	Jun	18	86.72	Aug	18	145.01	Oct	18	204.56	Dec	18	266.00
Feb	19	330.29	Apr	19	28.89	Jun	19	87.68	Aug	19	145.97	Oct	19	205.55	Dec	19	267.02
Feb	20	331.30	Apr	20	29.87	Jun	20	88.63	Aug	20	146.94	Oct	20	206.55	Dec	20	268.04
Feb	21	332.31	Apr	21	30.85	Jun	21	89.59	Aug	21	147.90	Oct	21	207.54	Dec	21	269.06
Feb	22	333.32	Apr	22	31.82	Jun	22	90.54	Aug	22	148.86	Oct	22	208.54	Dec	22	270.08
Feb	23	334.32	Apr	23	32.80	Jun	23	91.50	Aug	23	149.83	Oct	23	209.53	Dec	23	271.10
Feb	24	335.33	Apr	24	33.77	Jun	24	92.45	Aug	24	150.79	Oct	24	210.53	Dec	24	272.11
Feb	25	336.34	Apr	25	34.75	Jun	25	93.41	Aug	25	151.76	Oct	25	211.53	Dec	25	273.13
Feb	26	337.34	Apr	26	35.72	Jun	26	94.36	Aug	26	152.72	Oct	26	212.52	Dec	26	274.15
Feb	27	338.35	Apr	27	36.69	Jun	27	95.31	Aug	27	153.69	Oct	27	213.52	Dec	27	275.17
Feb	28	339.35	Apr	28	37.67	Jun	28	96.27	Aug	28	154.65	Oct	28	214.52	Dec	28	276.19
			Apr	29	38.64	Jun	29	97.22	Aug	29	155.62	Oct	29	215.52	Dec	29	277.21
			Apr	30	39.61	Jun	30	98.18	Aug	30	156.59	Oct	30	216.52	Dec	30	278.23
									Aug	31	157.55	Oct	31	217.52	Dec	31	279.25

Conferences

Thirty-Sixth International Meteor Conference, Petnica, Serbia, September 21–24, 2017

Dušan Pavlović[1] *and Nikola Božić*[1]

Introduction

As was already announced in the June issue of WGN, the 36th International Meteor Conference (IMC), will be hosted by the Petnica Science Center (PSC) in Petnica, a small village near the city of Valjevo (Serbia), from September 21 to 24, 2017. We are now in a position to give you more information and to invite you to participate!

After exactly twenty years, PSC has a privilege to host this event again. In 1997, hosting this event was of great significance for the activities of the Petnica Meteor Group, which organized meteor observations for years. Now, after decades of observing meteors, we hope that hosting the IMC will give at least the same tremendous boost to our activities, especially in the field of new observational techniques and their combination with visual observations and theoretical work.

As you will read, a lot has changed over these twenty years, and we hope that participation at the IMC 2017 will be as much instructive and enjoyable for all of you as for all the enthusiastic young people of Petnica Meteor Group and Petnica Science Center!

Conference dates

After the atypical dates of the IMC 2016 in Egmond, the Netherlands, the IMC 2017 returns to the traditional period, in the second half of September, more concretely from Thursday evening, September 21, till Sunday noon, September 24, 2017.

Organization and location

The IMC 2017 will be hosted by the Petnica Science Center, an extracurricular science education center for high school students (and, in recent times, for college students, too) from Serbia and abroad. It is located in Petnica, a small village near the city of Valjevo, about 100 km southwest of Belgrade. On the globe, you can find Petnica Science Center at 44°14′48″ N and 19°55′52″ E (Figure 1).

Figure 1 – Location of the Petnica Science Center.

[1]Petnica Science Center, Petnica, Valjevo, Serbia. Email: imc2017@imo.net.

Figure 2 – Panoramic overview of the PSC campus.

Those of you who attended the IMC 1997 will probably not recognize the site anymore, because the PSC campus has undergone a major expansion since then. The infrastructure has been significantly upgraded, and also the educational programmes offered have changed. The PSC campus today (Figure 2) includes several separate buildings, with more capacity for organizing and hosting different programmes. Therefore, PSC expanded its activities to include summer schools and workshops for undergraduate and graduate students from all over the world, as well as professional conferences.

Near PSC, there is a natural cave, a small artificial lake, a fish pond, and a sports center (with swimming pools and basketball, football, and volleyball courts, etc.).

Petnica has a humid continental climate. During the IMC, expect temperatures between 15° C and 30° C during daytime and between 5° C and 15° C at night.

Conference venue

The conference will be held at the Petnica Science Center (PSC) in Petnica, Serbia. The postal adress is *Petnica Science Center, P. O. Box 6, 14104 Valjevo, Serbia*, and the email address is `isp@petnica.rs`. You can find the PSC website at `http://www.petnica.rs`.

Since PSC is an extracurricular science education center in the middle of the countryside, its campus is a self-sufficient facility with all the necessary infrastructure for seminars and conferences, including separate buildings with lecture rooms and a conference room, laboratories, a library, a restaurant and a café, a small shop, a dormitory building, a big courtyard, and ample parking space.

The talks will be held at the conference room (Figure 3) in the main building, which has all the required facilities (beamer, projection screen, curtains for darkening, surround-sound speakers, air-conditioned and air-controlled) and a capacity of 150 people. Poster sessions will be held in the main hall (Figure 4) of the main building and in an adjoining lecture room. The whole area has a capacity of around 100 posters.

For the purpose of smaller meetings, open sessions, and workshops, participants are free to use several other lecture rooms (one with a capacity of around 50 people, just across the conference room, and several others in other buildings). There is also a computer room with 30 PCs, beamer, and whiteboard, and a library. Also, there is an open amphitheater in the courtyard of the campus with around 500 seats which can be used for the evening activities, a group photo, etc. The campus is covered by free WiFi Internet, and all bedrooms in the dormitory building also have LAN connectors.

Accommodation

The IMC 2017 participants will be accommodated on-campus at Petnica Science Center. Since all conference events will be hosted on-campus, there will be plenty of opportunity for the meteor community to interact at the conference, both formally and informally.

There are 14 single, 20 double, and 28 triple bedrooms (138 beds in total) available in the dormitory building (Figure 5), which is connected to the main conference building by a covered walkway. The dormitory building has elevators and chill-out/work rooms on every floor.

The separate building on the campus includes a restaurant (350 seats), a café, and a small shop. The restaurant (Figure 6) and café (Figure 7) open up to a nice terrace overlooking the area. Special food requirements can be arranged in advance, but, please, indicate this on the registration form.

If your travel plans are such that you arrive in Serbia before Thursday, September 21, or leave after Sunday, September 24, it is your responsibility to book the extra nights you require. It is possible to book extra nights at PSC before the start of the conference. For more information, please contact the Local Organizing Committee (LOC). Unfortunately, it is *not* possible to book extra nights at PSC after the conference because of other activities taking place at that time. We suggest that you look for alternative accommodation in either Valjevo or Belgrade, and the LOC will be glad to offer you assistance in doing so.

Figure 3 – The conference room, where the talks of the IMC 2017 will be held.

Figure 4 – The main hall will be reserved for the poster sessions.

Figure 5 – Dormitory building.

Figure 6 – Restaurant.

Although a no-accommodation option is provided on the registration form, we strongly recommend full-board accommodation at the Petnica Science Center. Nevertheless, if you want to have alternative accommodation, the LOC will be available for more information and recommendations. Mind, however, that, if you choose the no-accommodation option, you are responsible for transportation between your hotel and the conference location!

For more information about the costs involved, refer to the "registration and payment" section of this article.

Figure 7 – Café and small shop on the PSC campus.

Program and social events

The program will mainly consist of talks and poster sessions. The exact schedule will be determined shortly after the end of the registration period, when we get a clear picture of the number of speakers and topics. We anticipate that there will be both short talks and extended sessions, as well as workshops organized by the prominent specialists in various fields of meteor science. All presentations, both talks and posters, will be included in the IMC 2017 Proceedings as full-length papers or abstracts. As at the IMC 2016, there will be a contest for the best poster and the best meteor photo. You can find more information and instructions for these submissions on the IMC 2017 website.

Social events include evening activities, and on Saturday afternoon an excursion to the Valjevo surroundings will be organized. After the excursion, we will return to Petnica Science Center for dinner.

Registration and payment

We are able to offer the IMC 2017 at a most reasonable price, which is also good news for students.

The standard registration fee has been set at 130 EUR. This includes full board (accommodation in a triple bedroom, breakfast, lunch, and dinner) from Thursday evening September 21 (dinner included) till Sunday noon September 24 (lunch included), all lecture and poster sessions, conference materials, coffee breaks, and the Saturday afternoon excursion. Participants who wish to be accommodated in a double or single bedroom pay 170 EUR or 240 EUR, respectively. The no-accommodation fee is 75 EUR and includes the same as the standard fee, except for accommodation and breakfast. Again, we strongly recommend full-board accommodation at PSC.

T-shirts and printed proceedings can be both purchased separately upon registering. Electronic proceedings will be available for free to all participants.

The early-bird registration deadline is June 30, 2017. After Friday, 30 June 2017, a late booking fee of 20 EUR will be added to the registration fee. The final registration deadline is August 15, 2017. Mind though that registration may have to be closed earlier if full capacity is reached before August 15! Based on the number of beds available, the total number of participants is limited to 138, on a first-come first-serve basis. Accompanying persons older than 12 years sharing a room with a participant must also register as a participant.

Participants from outside Serbia pay either by International Bank Transfer or PayPal (including credit cards payments via PayPal). This does not apply to Serbian participants, however! Participants from Serbia have to pay in RSD and must check this payment option on the Registration Form. The LOC will then contact you with concrete payment instructions.

The cancellation policy for the IMC 2017 is as follows. Until June 30, 2017, there will be a full reimbursement, reduced with a cancellation fee of 15 EUR. Between July 1 and August 15, 2017, there will be a partial reimbursement of half of the registration fee, and from August 16, 2017, onward, there will be no reimbursement.

Please check the IMC 2017 website for more information and for registration.

Traveling to Petnica

Here, you will find some general information on how to reach Petnica. More detailed information will be available soon on the IMC 2017 website.

If you travel by plane, Valjevo can easily be reached via Belgrade Nikola Tesla International Airport. Once you arrive at the airport, you can either go by bus or by train to Valjevo, or you can rent a car and go directly to Petnica from the airport. If you want to rent a car, you can do that for a reasonable price at the airport. You can find a list of car rental agencies and more information about that option at the website of the airport. If you are using public transport, then first take a bus or taxi from the airport to the Belgrade central bus and train stations, and then a bus or train to Valjevo (see below).

If you travel by bus or train, go to Belgrade first and, there, take a bus or train to Valjevo from the Belgrade central bus and train stations (see below).

If you travel by public transport from Belgrade to Valjevo, you can either take a bus or a train. The central bus and train stations are all basically next to each other, and you can travel to Valjevo by bus from Lasta Bus Station or Belgrade Bus Station (BAS), or by train from Belgrade Railway Station. There are buses and trains from these stations to the Valjevo bus or train station approximately every hour. For more detailed information and actual timetables of bus and train departures, please check the IMC 2017 website. They will be available some time before the conference.

Free shuttle bus(es) from Valjevo to Petnica Science Center will be organized on Thursday. If you need this service, please indicate that on your registration form. After the registration is closed, more detailed information will be available.

If you travel by car, just follow the map which will be available at the travel information page on the IMC website. We encourage the participants to consider carpooling. By encouraging carpooling, we want to reduce the number of cars, lower the cost by sharing cars, and promote socializing while traveling to the IMC. The LOC will provide assistance with this.

For more travel information, please contact the LOC.

Shortly before and during the IMC, a telephone number will be active in case you have an emergency while traveling to Petnica. This number will be communicated to the participants in due time.

Website and contact information

More detailed information will be available shortly at the IMC 2017 web pages.

Please check `http://www.imo.net/conference-imc/next-imc` regularly, where a link to the IMC 2017 web pages will be provided as soon as they are ready. On the IMC 2017 web pages, you will also find all information on how to register, as well as the actual registration form.

The LOC is available for all questions at `imc2017@imo.net`. Via newsletters, the LOC will provide participants with more and more concrete information as the conference draws closer.

We are already looking forward to seeing you at the IMC 2017 in Petnica!

Meteor science

Confirmation of the delta Mensids (IAU#130, DME)

Peter Jenniskens[1], *Jack Baggaley*[2], *Ian Crumpton*[3], *and Peter Aldous*[4]

The CAMS New Zealand video meteor orbit survey detected a high southern declination meteor shower that was previously reported from radar and visual observations. This detection now confirms the delta Mensids (#130, DME) in the IAU Working List. The shower is most active between March 17–22, around the spring equinox.

Received 2016 November 13

During the routine reduction of CAMS New Zealand data from 2016 March (Jenniskens et al., 2016), a high declination meteor shower was detected that stands out well in sun-centered ecliptic radiant coordinates (Figure 1). The shower was also detected in 2015. 15 orbits cluster in time between solar longitude 353° and 6°, around the spring equinox. 11 of those meteors occurred between 357° and 2° solar longitude (March 17–22). Orbits are listed in Table 1.

Checking against the IAU Working List (Jopek et al., 2016) shows that the shower is known as IAU#130, the delta Mensids (DME), active from March 13 to March 21, in agreement with the time interval found here. Kronk (2014) gives a brief history. The shower was first reported by Gartrell (1972) from radar observations in Adelaide in 1969. His showers 3.04 and 3.05 with 11 and 10 measured trajectories, respectively, had a radiant at RA = 51°, Dec = −81°, $V_{\rm inf}$ = 34 km/s and RA = 50°, Dec = −78°, $V_{\rm inf}$ = 38 km/s, respectively, in good agreement with our video observations. Gartrell & Elford (1975) reported that the radar was in operation in the period March 16–22, with average activity centered on March 18 and 19, respectively. Visual observers have occasionally reported activity from this area during March 14–21, with a peak rate of 1–2 meteors per hour (Kronk, 2014).

This is the same shower as the beta Tucanids (#108, BTU), based on the source information given in Jenniskens (2006), who also pointed to McIntosh (1935) for a record of visual observations. However, the period of activity given for the BTU (Feb 27 – March 02) is earlier than derived from our observations, and the proposed parent body C/1976 D1 (Bradfield) would produce meteors earlier in the month (Table 1). Hence, the name beta Tucanids (#108, BTU) is best reserved for meteors from comet Bradfield.

Median radiant position and orbital elements from CAMS data are given in Table 1. The shower has a prograde 56.°9-inclined orbit with a Halley-comet like semi-major axis a = 4.2 AU. This appears to be dynamically evolved dust from a Halley-type parent comet contributing to the toroidal source. Specular radar observations often measure a shorter semi-major axis, in part because speed is measured downrange. Gartrell (1972) derived a shorter a = 2.13 AU orbit.

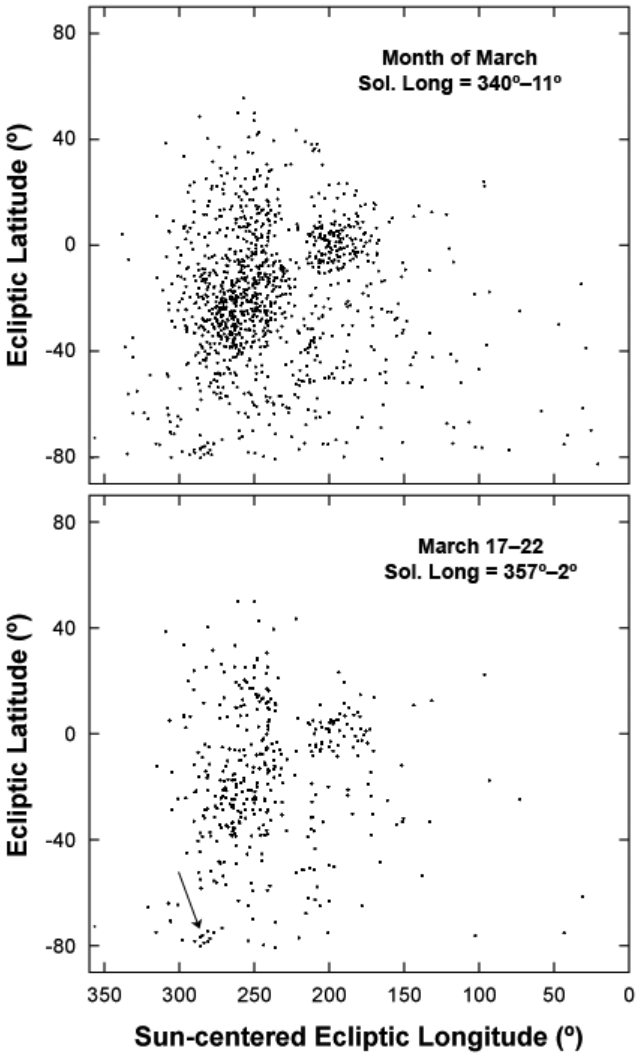

Figure 1 – Radiant distribution in sun-centered ecliptic coordinates for meteors detected in the month of March (top) and during the March 17–22 time interval (bottom). Arrow points to the newly confirmed delta Mensids.

Gartrell (1972) identified what might be the parent body: comet C/1804 E1 (Pons). The comet was only seen between March 7 and April 1 of that year, when it moved from near the equator at Libra into Bootes.

[1]SETI Institute, Mountain View, California.
Email: petrus.m.jenniskens@nasa.gov
[2]University of Canterbury, Christchurch, New Zealand.
[3]Canterbury Astronomical Society, West Melton, New Zealand.
[4]Geraldine Observatory, Geraldine, New Zealand.

IMO bibcode WGN-446-jenniskens-dme
NASA-ADS bibcode 2016JIMO...44..187J

Table 1 – Trajectory and lightcurve data of delta Mensids from CAMS data. $\lambda_\odot$ = solar longitude (J2000); RA_∞ and Dec_∞ are the Right Ascension and Declination of the apparent radiant; V_∞ is the apparent entry speed; a_1 and a_2 are deceleration parameters (Jenniskens et al., 2011); H_b and H_e are the beginning and end height; M_v is the absolute visual magnitude (for a distance of 100 km); F is the shape parameter of the light curve, being 0 when peaking at the beginning and 1 when peaking at the end; and Q is the convergence angle of planes between station and meteor.

Date	Time (UT)	$\lambda_\odot$ (°)	RA_∞ (°)	Dec_∞ (°)	V_∞ (km/s)	a_1 (km/s)	a_2 (1/s)	H_b (km)	H_e (km)	M_v (mag.)	F (°)	Q
2015/3/14	$12^h56^m57^s$	353.42	81.2	−79.8	32.7	0.037	0.362	107.8	80.7	1.4	0.37	14.2
2015/3/17	$17^h36^m06^s$	356.60	72.9	−81.6	37.2	0.722	0.169	103.6	87.5	0.9	0.76	39.8
2016/3/17	$15^h51^m49^s$	357.27	74.5	−80.9	35.2	0.000	0.120	102.8	93.9	1.8	0.94	31.3
2016/3/17	$17^h17^m22^s$	357.33	64.3	−78.4	32.0	0.210	0.274	102.2	97.3	2.0	0.25	79.1
2016/3/18	$12^h39^m32^s$	358.13	84.4	−78.1	38.9	0.027	5.992	102.7	83.9	−0.5	0.46	50.0
2016/3/19	$13^h02^m36^s$	359.14	79.6	−78.7	30.4	0.004	0.614	99.0	82.8	−0.3	0.51	16.6
2016/3/19	$13^h14^m50^s$	359.15	85.4	−80.0	36.7	0.037	0.036	105.0	88.7	0.9	0.90	37.3
2015/3/20	$11^h07^m37^s$	359.32	79.8	−81.7	36.0	0.034	0.114	104.7	90.5	1.2	0.54	33.5
2016/3/20	$08^h19^m12^s$	359.94	93.9	−82.6	36.8	0.034	0.325	103.3	88.7	0.9	0.70	36.2
2016/3/20	$10^h20^m08^s$	0.02	78.1	−79.8	34.5	0.155	3.660	104.3	95.8	2.3	0.54	77.5
2016/3/21	$11^h03^m28^s$	1.05	84.4	−81.6	36.5	0.018	0.100	105.9	91.4	0.1	0.67	35.1
2016/3/21	$12^h21^m14^s$	1.10	83.7	−78.6	37.7	0.020	9.643	106.8	87.7	1.0	0.75	40.3
2016/3/21	$15^h19^m36^s$	1.22	81.0	−77.8	31.5	0.001	4.975	109.2	85.6	2.3	0.87	46.5
2015/3/24	$16^h19^m42^s$	3.50	68.7	−77.2	36.1	0.014	0.135	107.1	86.2	−0.3	0.41	35.7
2015/3/26	$15^h53^m03^s$	5.47	65.8	−79.1	39.7	1.417	1.816	101.2	86.9	−0.8	0.27	4.6

Table 1 – (continued) – Geocentric radiant and orbital elements. RA, Dec, and V are now corrected for Earth's rotation and gravitational attraction. q = perihelion distance; a = semi-major axis; e = eccentricity, i = inclination, ω = argument of perihelion, Ω = node, Π = longitude of perihelion (J2000).

Date	Time	$\lambda_\odot$ (°)	RA_g (°)	Dec_g (°)	V_g (km/s)	q (AU)	$1/a$ (1/AU)	e	i (°)	ω (°)	Ω (°)	Π (°)
2015/3/14	$12^h56^m57^s$	353.42	73.9	−78.7	30.8	0.987	0.366	0.638	51.9	348.8	173.4	162.2
2015/3/17	$17^h36^m06^s$	356.60	75.9	−80.2	35.5	0.991	0.143	0.858	58.0	352.5	176.6	169.1
2016/3/17	$15^h51^m49^s$	357.27	73.5	−79.2	33.5	0.990	0.238	0.764	55.4	351.3	177.3	168.5
2016/3/17	$17^h17^m22^s$	357.33	67.2	−76.4	30.0	0.985	0.353	0.652	50.3	346.9	177.3	164.2
2016/3/18	$12^h39^m32^s$	358.13	79.7	−77.3	37.3	0.993	−0.099	1.099	58.0	354.5	178.1	172.6
2016/3/19	$13^h02^m36^s$	359.14	72.7	−77.1	28.4	0.990	0.457	0.548	48.7	349.4	179.1	168.5
2016/3/19	$13^h14^m50^s$	359.15	79.8	−79.0	35.1	0.994	0.127	0.873	56.9	354.7	179.1	173.8
2015/3/20	$11^h07^m37^s$	359.32	71.4	−81.2	34.3	0.992	0.272	0.730	57.5	352.2	179.3	171.5
2016/3/20	$08^h19^m12^s$	359.94	86.4	−83.3	35.1	0.996	0.292	0.709	59.5	357.3	179.9	177.3
2016/3/20	$10^h20^m08^s$	0.02	70.2	−79.5	32.7	0.991	0.310	0.693	55.0	351.0	180.0	171.0
2016/3/21	$11^h03^m28^s$	1.05	75.9	−81.2	34.8	0.994	0.235	0.766	58.1	354.6	181.0	175.6
2016/3/21	$12^h21^m14^s$	1.10	78.6	−77.8	36.1	0.994	0.015	0.985	57.3	354.9	181.1	176.0
2016/3/21	$15^h19^m36^s$	1.22	78.3	−75.7	29.5	0.993	0.342	0.660	49.3	353.0	181.2	174.2
2015/3/24	$16^h19^m42^s$	3.50	69.9	−75.5	34.4	0.991	0.069	0.931	54.7	351.2	183.5	174.7
2015/3/26	$15^h53^m03^s$	5.47	67.2	−77.7	38.1	0.993	−0.085	1.085	59.8	352.7	185.5	178.2
<median>		**356.60**	**73.9**	**−78.7**	**34.4**	**0.992**	**0.238**	**0.764**	**56.9**	**352.5**	**179.3**	**172.6**
C/1804 E1 (Pons)		**358.31**	**34.4**	**−73.2**	**34.9**	**1.071**	**0.000**	**1.000**	**56.5**	**332.0**	**179.5**	**151.5**
C/1976 D1 (Bradfield)		340.4	12.8	−63.5	32.9	0.848	0.007	0.994	46.8	313.0	160.8	113.8

The sparse observations suggested a long semi-major axis $a > 10$ AU. The calculated parabolic orbit has a perihelion distance $q = 1.071$ AU just outside of Earth's orbit, inclination $i = 56\,^\circ\!.45$, and node $\Omega = 179\,^\circ\!.53$ (J2000). The longitude of perihelion ($151\,^\circ\!.48$) is 21° from that observed for the meteoroids. The theoretical radiant is also $9\,^\circ\!.5$ from the observed radiant position.

Perhaps this reflects the dynamical evolution needed to cross Earth's orbit. If this was a Halley-type comet, it should have returned to perihelion at least once since 1804. Without further study, this association remains in doubt.

We thank Javor Kac for a constructive review of this article.

References

Gartrell G. (1972). "A southern hemisphere radio meteor orbit survey". *Proc. of the Astronomical Soc. Australia*, **2**, 89–90.

Gartrell G. and Elford W. G. (1975). "Southern hemisphere meteor stream determination". *Australian J. Phys.*, **28**, 591–620.

Jenniskens P. (2006). *Meteor Showers and their Parent Comets*. Cambridge University Press, 790 pages.

Jenniskens P., Baggaley J., Crumpton I., Aldous P., Gural P. S., Samuels D., Albers J., and Soja R. (2016). "A surprise southern hemisphere meteor shower on New-Year's Eve 2015: the Volantids (IAU#758, VOL)". *WGN, Journal of the IMO*, **44**, 35–41.

Jenniskens P., Gural P. S., Dynneson L., Grigsby B., Newman K. E., Borden M., Koop M., and Holman D. (2011). "CAMS: Cameras for Allsky Meteor Surveillance to establish minor meteor showers". *Icarus*, **216**, 40–61.

Jopek T. J., Koten P., and Pecina P. (2016). "IAU Meteor Data Center | the shower database: a status report". In *Proceedings of the Meteoroids 2016 meeting*. Planetary Space Science. (eprint arXiv:1607.00661).

Kronk G. W. (2014). *Meteor Showers: An annotated catalog, 2nd ed.* Springer Verlag, 60 pages.

Handling Editor: Javor Kac

Meteor Film Recording with Digital Film Cameras with large CMOS Sensors

Peter C. Slansky[1]

In this article the author combines his professional know-how about cameras for film and television production with his amateur astronomy activities. Professional digital film cameras with high sensitivity are still quite rare in astronomy. One reason for this may be their costs of up to 20 000 € and more (camera body only). In the interim, however,consumer photo cameras with film mode and very high sensitivity have come to the market for about 2 000 €. In addition, ultra-high sensitive professional film cameras, that are very interesting for meteor observation, have been introduced to the market. The particular benefits of digital film cameras with large CMOS sensors, including photo cameras with film recording function, for meteor recording are presented by three examples: a 2014 Camelopardalid, shot with a Canon EOS C 300, an exploding 2014 Aurigid, shot with a Sony α7S, and the 2016 Perseids, shot with a Canon ME20F-SH. All three cameras use large CMOS sensors; "large" meaning Super-35 mm, the classic 35 mm film format (24 × 13.5 mm, similar to APS-C size), or full format (36 × 24 mm), the classic 135 photo camera format. Comparisons are made to the widely used cameras with small CCD sensors, such as Mintron or Watec; "small" meaning 1/2" (6.4 × 4.8 mm) or less. Additionally, special photographic image processing of meteor film recordings is discussed.

Received 2016 November 15

1 Introduction

A classic (still) meteor photo shows the meteor as a streak. All information about the background sky is summed up over the integration time; all information about the meteor is summed up over the time and space of its angular movement over the sky. Hence in a single photo a lot of information about the meteor is lost: about the angular velocity of the meteor head, the temporal development of brightness and color of the meteor head and about trains and wakes (One part of this information, the angular velocity for example, can be saved in a still photo by the use of a rotating shutter in front of the lens.).

To record and preserve temporal information, cinematographic recording is one solution. Typically this is done with video cameras at 30 or 25 frames per second, depending on the television system, or by cameras attached to a computer with various frame rates. The resulting short integration time of typically 1/25 s to 1/30 s still does not give a frozen image, as it might seem, because the optical image of the meteor moves over the pixel pattern of the sensor during the integration time of the camera. In most cases the effective exposure time is limited by the meteor movement and not by the integration time of the sensor – just as in meteor still photography.

Figure 1 – This Camelopardalid was recorded by the author on 2014 May 24, $01^h58^m08^s$ UTC, in Munich, Germany, with a Canon EOS C 300 digital film camera with a Zeiss Superspeed Distagon 1.2/18 mm. The camera was running with 25 fps, $t = 1/25$ s, at ISO 20 000 with open iris. North is right. The image is cropped from a composite of 106 film frames, integrated with a maximum function. In the result the meteor appears as a streak. This is similar to a still photo with 4.24 s integration time ($106 \times 1/25$ s). Due to this integration over time, a lot of information about the temporal brightness and color development of the meteor head and of trains and wakes is lost. Compare this to Figure 3.

2 Camera technology

In meteor cinematography video cameras are normally used with one small monochrome charge coupled device (CCD) sensor. The main advantage of a CCD sensor is its comparably high sensitivity. The main disadvantage is the limitation in size and resolution: the widely used Watec 902H2 uses a 1/2" CCD sensor with a size of 6.4 × 4.8 mm and a native pixel count of 752 × 582. In order to keep the photo electrical effect efficient, the width and the height of the light sensitive area of a single pixel should be at least 5 times to 10 times of the wavelength of the light: 2.5 to 5 μm (Note, that usually the light sensitive area of a single pixel is only about 50% of the overall pixel area.). For a long time, CCD sensors for professional television cameras could not be built larger than for full HD resolution 1920 × 1080 pixels. The reason is that they have to be read out from as many vertical shift registers as the horizontal

[1]Hochschule für Fernsehen und Film München (University for Television and Film Munich, Germany).
Email: slansky@mnet-online.de

IMO bibcode WGN-446-slansky-film
NASA-ADS bibcode 2016JIMO...44..190S

Table 1 – Overview of cameras tested by the author.

	Canon C 300[1]	Sony α7S[2]	Canon ME20F-SH[3]
Camera type	Professional digital film camera	Consumer photo camera with film recording function	Ultra-high sensitive professional digital film camera
Cooling	active, balanced	passive, unbalanced	active, balanced
Sensor type	Color CMOS	Color CMOS	Color CMOS
Sensor size	22.5 × 12.7 mm	35.6 × 23.8 mm	35.6 × 20 mm
Sensor resolution	3840 × 2160 pixel	4240 × 2832 pixel	1920 × 1080 pixel
Native pixel size	6.25 × 6.25 μm	8.4 × 8.4 μm	19 × 19 μm
Recording resolution	1920 × 1080 samples	1920 × 1080 samples[4]	1920 × 1080 samples
Signal sample size	12.5 × 12.5 μm	19 × 19 μm	19 × 19 μm
Oversampling	2×	2.2×	none
Max. sensitivity	ISO 20 000[5]	ISO 400 000	ISO 4 000 000
Internal recording data format	MPEG-2	XAVC S	external recording only
Max. data rate	50 MBit/s (internal recording)	50 MBit/s (internal recording)	depending on external recorder
Lens mount	Canon EOS-mount or PL-mount	Sony E-mount[6]	Canon EOS-mount
Price (body only)	∼18 000 €[7]	∼2 000 €	∼19 000 €

[1] `http://www.canon.de/for_home/product_finder/digital_cinema/cinema_eos_cameras/eos_c300_pl/`
[2] `http://www.sony.de/electronics/wechselobjektivkameras/ilce-7s`
[3] `http://www.canon.de/for_home/product_finder/camcorders/multi-purpose-cameras/me20f-sh/`
[4] In film mode with internal recording; with external recorder max. 3840 × 2160 pixels at max. 30 fps possible.
[5] Sensitivity in 2014; after a firmware update in 2016 max. ISO 80 000.
[6] A lot of full format lenses of various manufacturers can be used via adapters.
[7] Price 2014; now Canon C 300 Mk II is on the market.

number of pixels into just one horizontal shift register at the bottom of the sensor, being the bottle-neck for the information distribution[a].

Complementary metal oxide semiconductor (CMOS) sensors do not have this limitation, because they have read out devices in every single pixel and a three-dimensional sensor structure for the (two-dimensional) sensor read out. In the last five years, technological progress has led to higher sensitivity and higher dynamic range. This makes such cameras more and more interesting for certain fields of astronomy, especially for meteor cinematography – in full color. In contrast with a professional broadcast camera, a digital film camera uses one large CMOS sensor with a Bayer pattern for RGB color detection instead of three small CCD sensors with an RGB optical beam splitter prism. The light distribution efficiency of a beam splitter prism system is about 90% of the incoming light. Compared with that, the Bayer filter matrix with light absorbing filter elements has an average light efficiency of about 30%. Nowadays, however, this disadvantage is more than compensated by the enormous increase of light sensitivity of the CMOS sensors themselves along with the implementation of highly efficient noise reduction algorithms into signal processing.

Most digital film cameras have CMOS sensors of the size of the classic 35 mm cine film cameras. "Super 35" means 24 mm × 13.5 mm at an image ratio of 16:9. This size is close to the APS-C format for digital photo cameras of about 22 × 12.5 mm. There are also full format cameras on the market with an image size of 36 mm × 20 mm (16:9), coming from the classic 135 photo format 36 × 24 mm.

Digital film cameras and digital photo cameras with film function have in common that film recording is done with a significant oversampling: Most digital film cameras use sensors with 1.5 times to 2 times more pixels horizontally and vertically than in the sampled signal. Oversampling does not mean binning: The real time down scaling is done by complex algorithms, comparable to advanced image processing software like Photoshop. The scaling ratio is not limited to integer numbers such as 2:1 or 3:1. The oversampling is also to compensate for the loss of resolution of a color sensor, compared with a monochrome sensor, caused by the Bayer mask[b]. It gives digital film cameras a smooth image without artifacts like aliasing or color aliasing. The oversampling ratio has to be taken for width and

[a] In the meantime professional broadcast cameras were introduced with 2/3" CCDs with native UHD resolution 3840 × 2160 pixels.

[b] In a color sensor with a Bayer mask half of the sensor pixels are filtered in Green, a quarter in Red and another quarter in Blue. To reconstruct all three primaries for every sample of the signal, the native signal from the sensor has to be "de-bayered". For this, the information of two green sensor pixels, one red and one blue sensor pixel sensor are combined. This causes an average loss of resolution of the sampled signal compared to the native sensor resolution of 0.63×, horizontally and vertically. This loss can be compensated by an oversampling with 1.6 times (1/0.63×) more pixels horizontally and vertically.

height, so a 2:1 oversampling means four times more native pixels on the sensor than recorded samples in the signal. For example, the Canon EOS C 300 has a color CMOS sensor with a Bayer mask with a native resolution of 3840 × 2160 pixels. The native signal from the sensor is de-bayered and downscaled in real time, resulting in a full HD signal with 1920 × 1080 samples being recorded. That means an overall number of 2 200 000 samples[c] per image. Compared with still photography cameras with up to 30 Megapixels this may sound mediocre, but full HD resolution is five times the pixel count of standard definition video (SD) with 440 000 pixels per image, being provided by cameras like the Mintron MTV-12V6HC-EX or the Watec 910HX-RC (without oversampling).

All three cameras have UV/IR cut filters. In the Canon ME20F-SH it can be deactivated motorized. All three cameras run from 2 frames per second (with frame integration) up to 60 fps.

Professional digital film cameras and digital photo cameras with film mode offer another valuable advantage over conventional video cameras: a significant wider contrast range. The contrast transfer function can be adjusted manually or via a set of different gamma presets: All three cameras offer "cine gamma" (whilst naming it differently), giving a very flat contrast distribution characteristic[d].

3 Camelopardalid 2014 May 24, $01^h58^m08^s$ UTC, from Munich, Germany, shot with Canon EOS C 300

At the Munich University for Television and Film (HFF), several professional digital film cameras with large CMOS sensors are in use for the student films – but sometimes even the professor for film technology is allowed to borrow one of them.

Figures 1 and 3 are the results of my first film meteor recording with a professional digital film camera. Figure 3 was chosen for the cover of the *WGN, Journal of the IMO* 42:3 (2014) – a great honor for me, being an amateur astronomer. My scientific approach was a technological one: to test the possibilities of this type of camera for meteor recording and imaging.

The Camelopardalid sequence that I captured was shot with a Canon EOS C 300, equipped with a Zeiss Superspeed Cine Distagon 1.2/18 mm, in Full HD resolution 1920 × 1080 pixels at $F = 1.2$ and ISO 20 000 with 25 frames per second and 1/25 s integration time. Hence every frame represents an interval of 1/25 s or 40 ms. On my rooftop terrace in the Munich city center

Figure 2 – The instrumentation for the Camelopardalid 2014 May 24, $01^h58^m08^s$ UTC, Figures 1 and 3 was a Canon EOS C 300 with a Zeiss Cine Superspeed Distagon 1.2/18mm on a Lichtenknecker M 100 B mounting on my rooftop terrace in the Munich city center, Germany.

the camera was put onto a mounting. The motors remained switched off. The camera was pointed near the zenith, with Polaris and Vega in the picture. Recording was started shortly after midnight, then I went to bed. The resulting 2½ hours film sequence showed only one meteor: the bright Camelopardalid at $01^h58^m08^s$ UTC in Figures 1 and 3.

The Camelopardalid flew almost North to South, so its track went nearly parallel to the long side of the 16:9 image (North is right in Figures 1 and 3). Peter Jenniskens and Jim Albers from the SETI institute, California[e], sliced narrow strips from the frames of my original film sequence and put them one under another to a compositing image. To this composite I added a numbering for each frame. From the first appearance of the meteor to its maximum brightness Jenniskens/ Albers took only every second frame, from the maximum brightness to the vanishing of the train they took every frame. This change of the vertical scale (the time scale) causes a "virtual knee".

In the following diagram, the image was numbered by me from frame to frame to show the exact timing. It starts with $t = 0$: The frame before the meteor is detected by the camera. The maximum brightness is at frame 27 ($t = 1.08$ s). Already, however, at frame 17 ($t = 0.68$ s) the meteor shows an orange train that keeps glowing for more than three seconds until frame 106[f]. The meteor itself gets darker from frame 27 until it vanishes at frame 75 ($t = 3$ s). As Peter Jenniskens describes, from frame 50 ($t = 2$ s) the meteor becomes slower, as can be seen by the curvature in the image. Unlike the "virtual knee", caused by the change of the vertical time scale, this is a real effect: The meteor heats up, breaks into very small pieces and slows down until it vanishes. In the meantime, the glowing train keeps visible for more than another second, until frame 106.

The brightest visible stars in the original film sequence are Vega (0.1 mag) and Deneb (1.3 mag), the

[c] In a signal the correct term for what is called "pixel" in common speech is "sample". Hardware devices like sensors or displays have pixels, signals have samples.

[d] A classic video camera usually is set up to a logarithmic contrast transfer function with gamma = 0.45, according to CCIR Recommendation 601 (SD) resp. ITU Recommendation 709 (HD). This results in a contrast range of max. 7 F-stops or 128:1 (Slansky & Möllering, 1993). Measurements by the author have approved a maximum contrast range for the Canon C 300 up to 11 F-stops and for the Sony α7S up to 13 F-stops.

[e] `http://meteor.seti.org`

[f] It was this orange train that attracted Peter Jenniskens' special interest

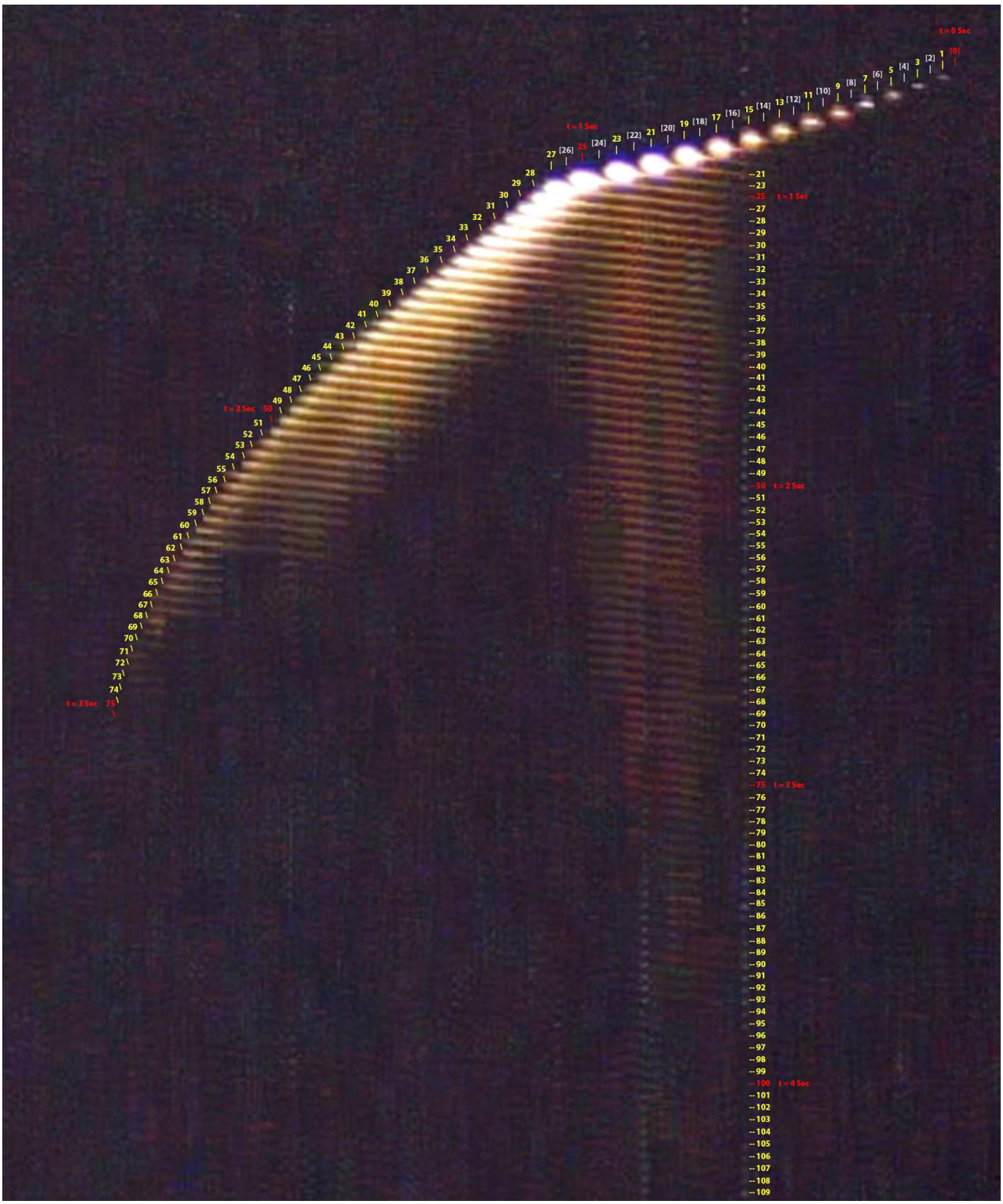

Figure 3 – Camelopardalid on 2014 May 24, $01^{h}58^{m}08^{s}$ UTC, from Munich, Germany, from same original film sequence as Figure 1, shot with a Canon EOS C 300 digital film camera with a Zeiss Superspeed Distagon 1.2/18mm. The sensor size is 22.5 × 12.7 mm. The camera was running with 25 fps, $t = 1/25$ s, at ISO 20 000 with open iris. North is right. The compositing was done by Peter Jenniskens and Jim Albers, SETI Institute, Los Angeles, USA (Jenniskens, 2014). It shows each film frame displaced by 5 pixels vertically, projected in such a way that the meteor moves from right to left. The vertical direction from top to bottom is the timeline. The numbering of each film frame (= 1/25 s; yellow) and of each film second (every 25th frame; red) was done by the author. The sequence starts with an interval of only every second film frame to be shown for the first second. The jumped frames are marked with white numbers in brackets. After one second the sequence continues with every film frame to be shown until the end at frame No. 109 ($t = 4.36$ s). Only because of this change of the scale of vertical timeline, there is a "virtual knee" in the curve at frame No. 26. From the top to the bottom this sequence shows the temporal development of the meteor frame by frame: the persistent emission and wake as well as the deceleration when the meteoroid breaks. Also, the temporal development of the meteor brightness can be estimated: The star slightly left from the vertical number column, marked in green, is χ Draconis (3.7 mag). Additional information is provided by the development of the colors of the meteor head, persistent train and wake. Compare this to Figure 1. The author offers this information to the scientific meteor community, leaving conclusions – for example brightness estimations – to the expert.

faintest are 24 Draconis (5.0 mag) and 30 Draconis (5.2 mag). Note, that the faintest stars can only be seen in the original film sequence running at 25 fps: In a single still frame resp. in Figure 3 they vanish in the image noise. This makes it difficult to prove the limiting star magnitude in a print copy. Modestly estimated, the limiting star magnitude of the film sequence can be assumed with mag 5.2. This is not very far from the (poor) sky darkness of the observation site in the center of Munich. In Figure 3 a star is visible (marked in green): χ Draconis, mag 3.7. Considering all these factors it would be possible to determine the magnitude of the meteor. For this further research has to be made.

The film sequence can be seen here:
`http://slansky.userweb.mwn.de/bereiche/astronomie/meteore/camelopardalid_24-05-2014_ani_k.html`.

4 Exploding Aurigid 2014 September 1, $05^h44^m44^s$ UTC, from La Palma, Canary Island, shot with Sony α7S

With a maximum sensitivity up to ISO 400 000, the Sony α7S is by far the most light sensitive camera for photo and film mode in a price range of 2 000 € (body only) at the moment. It has a full format CMOS sensor 35.5×23.5 mm with a native resolution of 4240×2832 pixels and a native pixel size of 8.4×8.4 μm. In film mode the active sensor area is cropped to 35.5×20 mm (16:9). With internal film recording it is down sampled to full HD resolution of 1920×1080 pixels, with a sample size of 19×19 μm. Connected to an external data recorder via the micro HDMI 1.4 interface, film recording is possible up to UHD resolution 3840×2160 Pixels at max. 30 fps, depending on the recorder. The Sony E lens mount has a very short camera flange back distance, so it is possible to adapt nearly every full format lens to the α7S via third party adaptors.

One major disadvantage of the Sony α7S for meteor recording is that, being a consumer photo camera instead of a professional film camera, the maximum film recording time is limited to less than 30 minutes. This was implemented by the manufacturer due to toll regulations that provide a lower tax rate for consumer photo cameras than for professional film cameras. It can only be prevented by using an external recorder.

The exploding Aurigid fireball in Figure 4 was recorded on 2014 September 1 at $05^h44^m44^s$ UTC from my hotel balcony at La Palma, Canary Island, about 40 m above sea level. The Sony α7S was equipped with a Zeiss ZE Sonnar 2.8/35mm. The camera was put onto a tripod and pointed to North by Northwest. The film sequence was recorded with 25 fps with $t = 1/25$ s, ISO 200 000 and $F = 2.8$.

The frame by frame composite image Figure 4 (left) shows how the meteor enters the image field from right to left at frame No. 2 with a constant angular speed. The meteor head is strongly overexposed, but the following wake is not. At frame No. 7 the meteor head disintegrates completely in an abrupt explosion. A greenish train can be seen for about 1 s. The white afterglow of the explosion remains visible for more than 10 s, exceeding by far the range of this sequence analysis of 55 frames (= 2.2 s) until the bottom of Figure 4 (right). The changing of the colors of the train and the explosion cloud can be studied easily frame by frame.

The film sequence can be seen here:
`http://slansky.userweb.mwn.de/bereiche/astronomie/meteore/aurigid_01-09-2014_ani_k.html`.

5 Perseids 2016 August 12/13 from Emberger Alm, Austria, shot with Canon ME20F-SH

In 2015 Canon presented an ultra-high sensitive professional film camera with a maximum sensitivity of ISO 4 000 000, the Canon ME20 F-SH. It has no internal recording nor a viewfinder nor a display, all needs to be attached externally. It has a full format CMOS sensor with a native resolution of full HD 1920×1080 Pixels, resulting in a pixel size of 19×19 μm, the biggest native pixel size on the market right now. Together with an advanced noise reduction system, this is the key to the extraordinary sensitivity. The sensitivity of the ME20 F-SH can be switched from 0 dB by gain steps of 3 dB. +6 dB mean an increase of one F-stop or a factor 2 for the ISO number, +3 dB means half an F-stop or factor 1.4. The maximum sensitivity of +75 dB is stated to be equivalent to ISO 4 000 000. For this goal, the manufacturer has sacrificed smoothening of the image by oversampling.

Unfortunately, the Canon ME20F-SH is out of reach for most amateur astronomers due to its price of 19 000 € (body only). The need for an external data recorder with a display and a separate power supply does not make the handling very comfortable. However, the ME20 has no recording time limit, unlike consumer cameras like the Sony α7S.

For the 2016 Perseids observing campaign, the author and Bernd Gährken, also from Munich, went to Emberger Alm in the southern Austrian Alpine Mountains at 1 740 m above sea level. Two Canon ME20F-SHs, equipped with Canon USM II 1.4/35 mm photo lenses, were provided by Canon Germany Ltd., Krefeld. These two cameras, together with two Sony α7S with 2.8/35 mm Zeiss lenses, were mounted on a Lichtenknecker M 100 B mounting. Two data recorders Ambient PIX 240i were connected to the Canon cameras. All cameras were pointed to Polaris, covering the same sky area simultaneously. The sensitivity was set up differently from camera to camera via ISO number and F-stop. This setup was chosen to compare the cameras on the same motive and for a direct measurement of the population index, the topic of another article yet to come.

Molau et al. (2014) have pointed out that the simple detection of faint stars in the image is not a very reliable criteria for the limiting star magnitude. But it does give a first draft. They tested a Mintron 12V6-EX against a Watec 910HX-RC: Under a mag 6.0 sky and with a 0.75/6 mm Panasonic lens the Mintron reached a limiting star magnitude 5.1 and the Watec mag 5.5. Many cameras of the IMO Video Meteor Network do not reach this magnitude.

Peter Jenniskens (2014) used Night Vision MX-9916/UV image intensifier tube cameras for the 2014 Camelopardalid campaign from an airplane at an altitude of 6 000 to 8 000 m, reporting a limiting star magnitude 6.9. With the Canon ME20F-SH, set to ISO 1 400 000, $F = 2.0$ and 25 fps, $t = 1/25$ s, a limiting star magnitude was reached up to mag 8.6.

The star detection as well as the meteor detection was performed "manually" by playing back the original film sequences in real time on a computer monitor; no detection software was used. The image presented in Figure 7 was summed up from 100 film frames and cropped from the original full HD resolution.

On the first night, 2016 August 11 to 12, the cameras were running from 23^h09^m to 02^h01^m UTC. During these 2:52 hours the most sensitive Camera 1, a Canon ME20F-SH, recorded an overall of 266 meteors, among them 224 Perseids. On the second night, August 12 to 13, the cameras were running from 21^h35^m to 01^h21^m UTC. Despite some

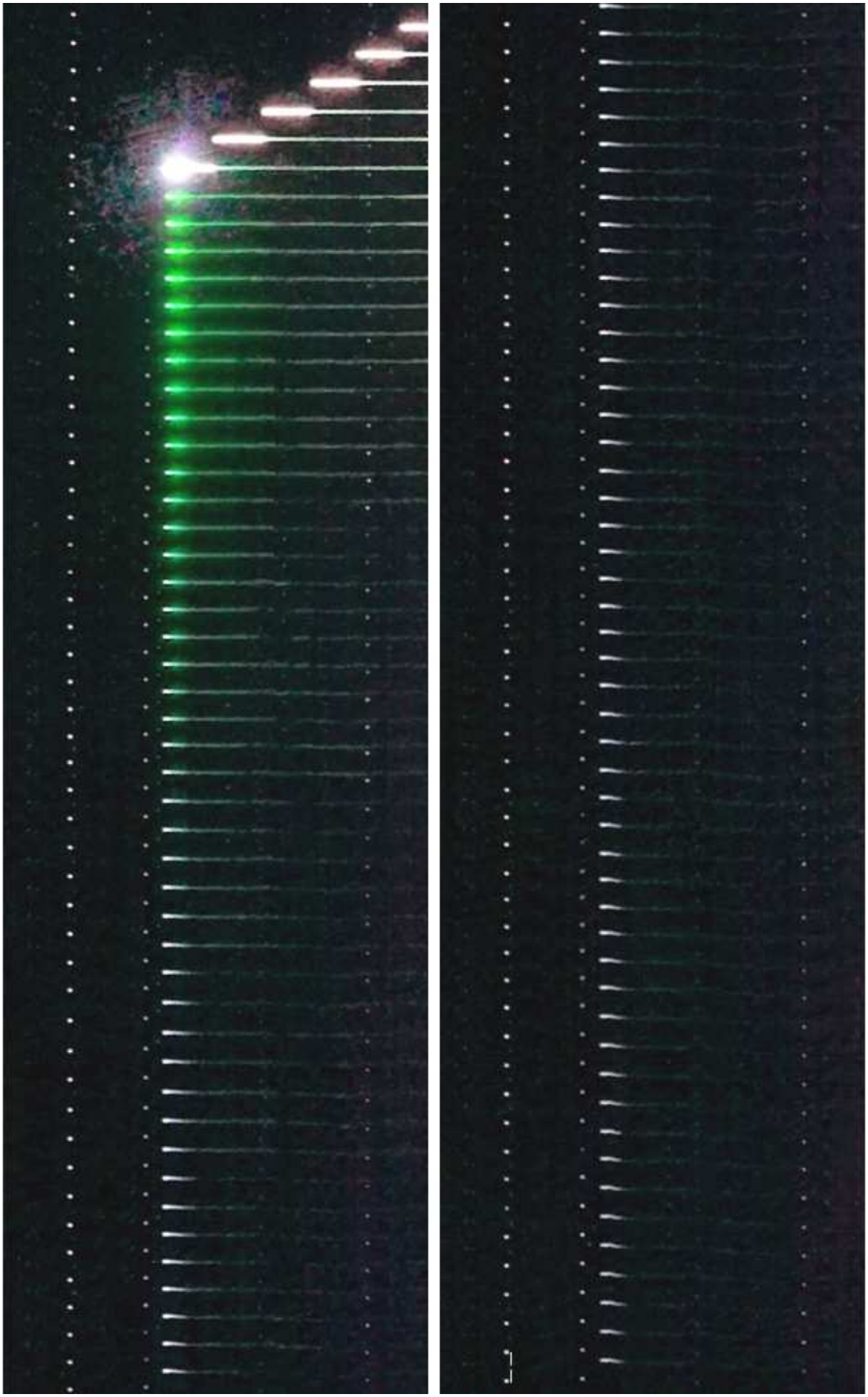

Figure 4 – Exploding Aurigid fireball on 2014 September 1, $05^{h}44^{m}44^{s}$ UTC, from La Palma, Canary Island. The original film sequence was shot with a Sony α7S with a Zeiss ZE Sonnar 2.8/35 mm. The camera was on a tripod, pointing to North by Northwest. The film sequence was recorded with 25 fps with $t = 1/25$ s, ISO 200 000, $F = 2.8$.

Figure 5 – 45 Perseids 2016, composite image with maximum function. The star in the image center is Polaris, Ursa Minor is left. The original film sequence was shot with a Canon ME20F-SH with a Canon USM II 1.4/35 mm lens. It was recorded with 25 fps, $t = 1/25$ s and ISO 1 400 000 at $F = 2.0$.

Figure 6 – Instrumentation for the 2016 Perseids, Figures 5, 7 and 8. Two Canon ME20F-SH cameras and two Sony α7S were mounted on a Lichtenknecker M 100 B, with an image field rotating around the sky North Pole. The location is Emberger Alm in the Austrian Alpine Mountains, 1 760 m above sea level. On the bottom of the mounting (not in the picture) two data recorders were connected to the Canon ME20 cameras. Over all, ten AC power supplies were needed.

Figure 7 – Composite image of 100 film frames of the brightest Perseid on 2016 August 11/12, $01^{h}29^{m}33^{s}$ UTC, from Emberger Alm (at the bottom right in Figures 5 and 8). Due to the average function of the compositing, the green train of the meteor is prominent while the bright overexposed meteor head is nearly invisible. Modestly estimated, stars down to mag 8.6 can be identified – also in the original film sequence when running at 25 fps.

clouds passing the field of view, in 3:43 hours an overall of 247 meteors were recorded by Camera 1, among them 163 Perseids. For the whole campaign with 6:35 hours recording time in two nights, this makes an overall of 513 meteors, among them 387 Perseids.

The original data amount of all four cameras was 740 GB, 240 GB for each Canon ME20 and 130 GB for each Sony α7S. Image processing and analysis are not yet finished.

Images and film sequences can be seen here: `http://slansky.userweb.mwn.de/bereiche/astronomie/meteore/perseiden_2016_01.html`.

6 Film image processing

As was explained earlier, a film sequence contains much more of the temporal information about a meteor than a still photo. A part of this information can be transformed back into a still image, for a printed article for example, by special image processing. For this, film editing software as well as astronomical imagery software is needed.

To show just one example, two composite images of the brightest 45 Perseids of the first night from the same source image sequence will be compared: Figure 5 and Figure 8.

The data recorder Ambient PIX 240i recorded in the professional video codec ProRes in 8 Bit per channel. The ProRes sequences were imported into a professional film editing software, Adobe Premiere CC 2015. For each of the 45 meteors, a sequence of 100 film frames (= 4 s) was exported in TIF 8 Bit RGB. These TIF sequences were the key to the astronomical imagery in Fitswork 4.47 and the compositing in Photoshop CC 2015.

Figure 5 shows the composite of the 45 brightest 2016 Perseids from August 11, $23^h10^m10^s$ UTC to August 12, $01^h59^m02^s$ UTC. The emphasis was laid on the bright meteor heads by a composite of 45 composites: Each meteor sequence of 100 frames was composed in Fitswork 4.47 with the maximum function. The maximum function transfers the maximum brightness value of all 100 frames for each pixel into the resulting composite. Due to the very high sensitivity of the camera of ISO 1 400 000, $F = 2.0$, $t = 1/25$ s, most of the meteor heads are strongly overexposed. This causes a noticeable blooming. In a second step the 45 maximum composites were combined in Photoshop to a 45-layer composite and combined again with the maximum function. The resulting image Figure 5 shows the bright tracks of each meteor head. With this method of image compositing, much of the original image noise is visible. The colors of the meteors are nearly invisible because of the overexposure of the meteor heads. This composite does however offer an initial estimate for the magnitude of the meteors.

Figure 8 shows the same 45 Perseids, but with the compositions in the first step being made via the average function. As a result of this, the persisting trains of each meteor are displayed in their typical green color. Because at on every pixel the bright meteor head is apparent only for one frame from 100, its value is lowly weighted by the average function, compared to the sky background. The trains remain for at least one second, up to several seconds, so the averaging of 100 frames results in a strong emphasis on them.

Figure 8 – Composite image of 45 Perseids 2016; same sequence as Figure 5, but composite made with an average function. By this, the green persistent trains are dominant and the bright meteor heads are pushed into the background.

The comparison between these two composites from the same original source shows the various possibilities of meteor film recording in full HD resolution and color. More research about these possibilities seems to be valuable.

Acknowledgements

I wish to thank Barbara Arriens from Canon Germany Ltd., Krefeld, for providing me with two brand new ME20F-SH cameras with lenses for the 2016 Perseid campaign. I thank the University of Television and Film Munich for providing me with the cameras for the 2014 Camelopardalids and the 2014 La Palma fireball. I also wish to acknowledge considerable cooperation with Bernd Gährken and his preparations and the weather prediction for the 2016 Perseid campaign and for his help with the analysis. Also, I want to thank Sirko Molau, who gave his advice in the systematic of the 2016 Perseid campaign. Very important input has also been given by Matthias Knülle, especially to the choice of the lenses. I thank Peter Jenniskens for his valuable response to the 2014 Camelopardalid, my initial meteor film recording, and for his analysis. Last but not least, I thank Daniel Fischer for his initiative to forward the information about my Camelopardalid film sequence to the scientific community, finding Peter Jenniskens.

References

Jenniskens P. (2014). "Camelopardalids (IAU#451) from comet 209P/LINEAR". *WGN, Journal of the IMO*, **42:3**, 98–105.

Molau S., Kac J., Crivello S., Stomeo E., Barentsen G., Goncalves R., and Igaz A. (2014). "Results of the IMO Video Meteor Network – March 2014". *WGN, Journal of the IMO*, **42:3**, 120–124.

Slansky P. C. and Möllering D. (1993). *Handbuch der Professionellen Videoaufnahme*. Edition Filmwerkstatt, Essen.

Handling Editor: Felix Bettonvil

Preliminary results

Results of the IMO Video Meteor Network — June 2016, and photometry algorithms

Sirko Molau[1], *Stefano Crivello*[2], *Rui Goncalves*[3], *Carlos Saraiva*[4], *Enrico Stomeo*[5], *and Javor Kac*[6]

A total of 75 cameras of the IMO Video Meteor Network recorded nearly 22 000 meteors in almost 7 000 hours of observing time in 2016 June. A case of photometry of an object recorded on an uneven background is discussed.

Received 2016 November 24

1 Introduction

June excelled with perfect observing conditions. A quick look at the statistics shows only few gaps with a highlight on June 6/7, when 67 out of 75 cameras were active. Only in Slovenia and parts of Germany the weather was mediocre, otherwise most cameras enjoyed great conditions. In the end we counted fifty cameras with twenty or more observing nights and one camera (Lic1) which observed without any break at all.

With respect to the total effective observing time we fell only about 3% short of the result from 2015. On the other hand, it was for the first time that we recorded more than 20 000 meteors in June (Table 1 and Figure 1), which is an increase by 15% relative to the previously best result.

2 Minor showers of June

With respect to the meteor showers, June represents the "calm before the storm". The average hourly meteor rate has already increased by 50% relative to the annual low in March, but the nights are very short in the northern hemisphere and there is a lack of meteor showers.

You have to observe an average of ten hours in the small morning observing window to catch one Daytime Arietid, for example, and even then it could be a sporadic meteor that aligns only by chance with the shower radiant. In other words, only every other camera managed to record a single Daytime Arietid in this season.

The observing geometry for the June Bootids is much better, since the radiant is circumpolar in central Europe and lies close to the zenith at the beginning of night. Hence, we have a large effective collection area for this shower and would be able to detect even the lowest shower activity with a ZHR below 1 in our video data, but as in recent years the shower was not active in 2016.

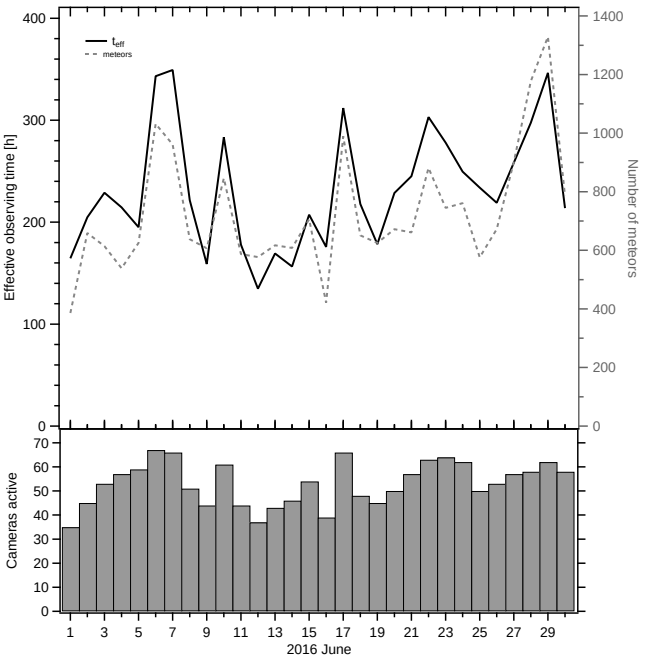

Figure 1 – Monthly summary for the effective observing time (solid black line), number of meteors (dashed gray line) and number of cameras active (bars) in 2016 June.

3 Photometry algorithms

Let us once more address the algorithms of video meteor observation. In the March report (Molau et al., 2016) we presented, how the angular meteor velocity affects the meteor limiting magnitude of a camera. The only parameter of this model, which assumes that stars and meteors are radial-symmetric Gaussians, is the variance of the Gaussian distribution. This has to be estimated for every video camera from images.

Before we have a closer look at the algorithm to determine the variance, let us first consider a particular problem we encountered when developing the algorithm. Whenever we are calculating brightnesses, we obtain the pixel sum of an object (star, meteor). At first, the background brightness is determined at the location of the object, then all pixels belonging to the object are selected (those which are connected to one

[1]Abenstalstr. 13b, 84072 Seysdorf, Germany.
Email: sirko@molau.de
[2]Via Bobbio 9a/18, 16137 Genova, Italy.
Email: stefano.crivello@libero.it
[3]Urbanizacao da Boavista, Lote 46, Linhaceira, 2305-114 Asseiceira, Tomar, Portugal. Email: rui.goncalves@ipt.pt
[4]Rua Aquilino Ribeiro, 23 - 1 Dto. 2790028 Carnaxide, Portugal. Email: carlos.saraiva@netcabo.pt
[5]via Umbria 21/d, 30037 Scorze (VE), Italy.
Email: stom@iol.it
[6]Na Ajdov hrib 24, 2310 Slovenska Bistrica, Slovenia.
Email: javor.kac@orion-drustvo.si

IMO bibcode WGN-446-molau-vidjun
NASA-ADS bibcode 2016JIMO...44..199M

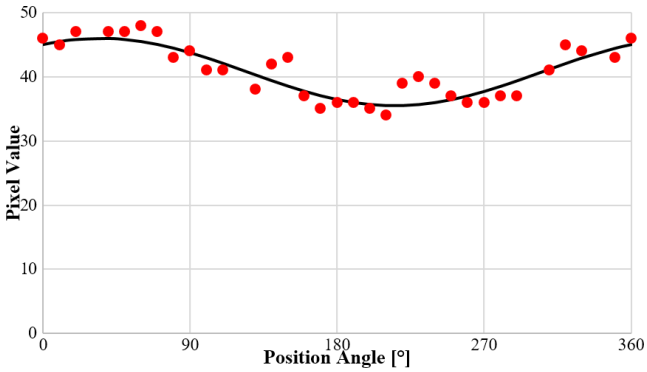

Figure 2 – Pixel values around a star in an image-intensified camera with brightness gradient (dots), and the corresponding sine function (line).

another and which are by a certain amount brighter than the background) and finally these pixel values are accumulated after subtracting the background. The background brightness is determined by aperture photometry. The average brightness of all pixels along a close circle around the object is calculated, omitting particularly bright (e.g. nearby stars) and faint pixels (e.g. dust at the sensor).

Aperture photometry works fine for Mintron and Watec cameras which have a uniform background. However, image-intensified cameras often show a strong background brightness gradient, making up for several gray levels even within the small area around an object. That is not an issue for the calculation of the background brightness, because the values of all pixels around the objects are averaged. However, it may happen that the background pixels at the brighter edge of the object are beyond the threshold and thus counted as belonging to the object. The impact is small for photometry, but it hurts the algorithm to estimate the variance which will be presented below, since these pixels have a large distance from the object center and consequently a big weight.

Now the procedure is improved such that the local brightness gradient around the object is detected and accounted for. The simplest form is a linear gradient with constantly increasing brightness in one defined direction. Since we are looking at only a small area around the object, that model is sufficiently precise. If the brightness of the pixels along a circle around the object is plotted against their position angle relative to the object center, they will follow a sine function if a linear gradient is present. Now the task is to fit a sine function to the observed pixel values and determine the direction and strength of the gradient.

Figure 2 shows the pixel values around a star from an image-intensified camera (Figure 3, left) and a fitted sine curve with an amplitude of $A = 5.2$ and a phase angle of $\varphi = 305°$.

Since the frequency of the sine function is well-known (the pixels originate from a circle around the object and thus cover exactly 360°), we can use a simplified presentation for the sine function:

$$h = A \sin(x + \varphi) + O \tag{1}$$

where h represents the pixel brightness, A the amplitude of the brightness gradient, x the position angle relative to the object center, φ the phase angle (which defines the direction of increasing brightness) and O the offset. O is simply the average pixel value – the only unknown factors are the searched values A and φ. A quick online search revealed that in this simplified case with known frequency there is no need for an iterative parameter estimation, but there exists a closed-form solution to determine the best parameters with least mean squared error. In order to do so, we represent Equation 1 in a different form

$$h = a \sin x + b \cos x \tag{2}$$

whereby the searched values A and φ can be calculated as follows:

$$A = \sqrt{a^2 + b^2} \tag{3}$$

$$\varphi = \tan^{-1}\left(\frac{b}{a}\right) \tag{4}$$

In Equation 2 we can determine a and b independently by linear regression. The corresponding Equations 5 and 6 look complicated, but they can be implemented with just a few lines of code and require no expensive iterative optimization:

$$a = \frac{\Sigma_n(\cos x_n)^2 \Sigma_n h_n \sin x_n - \Sigma_n \sin x_n \cos x_n \Sigma_n h_n \cos x_n}{\Sigma_n(\sin x_n)^2 \Sigma_n(\cos x_n)^2 - (\Sigma_n \sin x_n \cos x_n)^2} \tag{5}$$

$$b = \frac{\Sigma_n(\sin x_n)^2 \Sigma_n h_n \cos x_n - \Sigma_n \sin x_n \cos x_n \Sigma_n h_n \sin x_n}{\Sigma_n(\sin x_n)^2 \Sigma_n(\cos x_n)^2 - (\Sigma_n \sin x_n \cos x_n)^2} \tag{6}$$

Once the phase angle and amplitude of the brightness gradient are calculated for the object, the calculation of pixels that belong to the object is not any more based on the average background brightness O, but rather on the local background brightness at the position of the pixel estimated by Equation 1.

The result will be presented for two cameras. Figure 3 shows on the left side a recording from the image-intensified camera Avis2 with a strong brightness gradient, and on the right side from an ordinary Mintron (Mincam1) without brightness gradient.

In Figure 4 we calculated the phase and amplitude of the brightness gradient for each pixel and presented the result as vector graphics. The direction of the vector represents the direction of increasing brightness and the length of the vector represents the amplitude. It can be seen that the background brightness of the image-intensified camera increases and decreases radial-symmetrically from the center, whereas there is no clear brightness gradient for the Mintron camera.

In Figures 5 and 6, the phase angle and amplitude information is displayed independently. In case of the phase angle (Figure 5, encoded with gray levels), the image-intensified camera shows the expected radial-

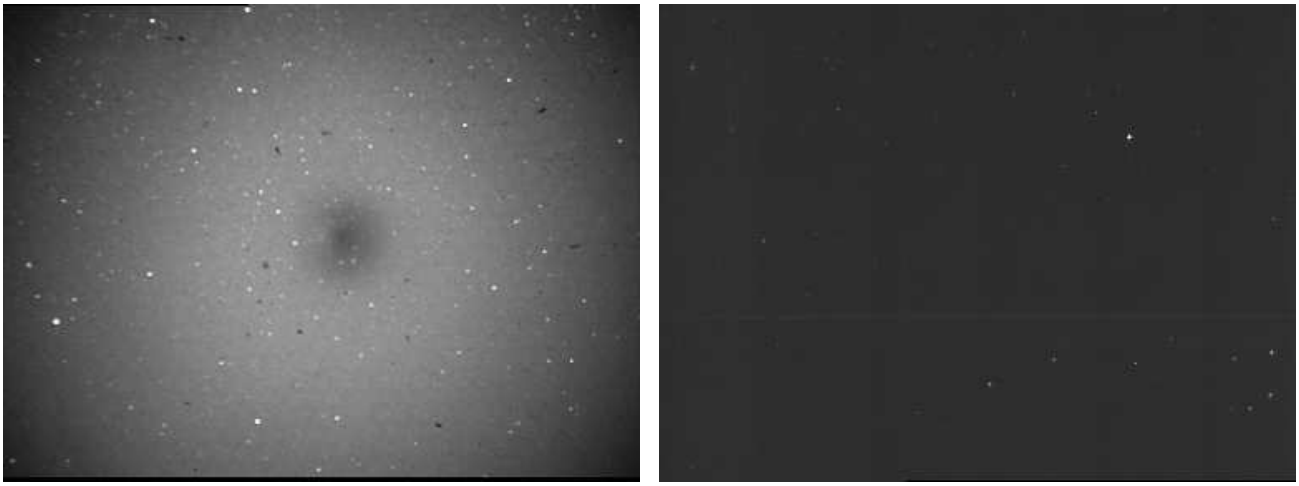

Figure 3 – Recordings of an image-intensified camera with brightness gradient (left) and of a Mintron camera without brightness gradient (right).

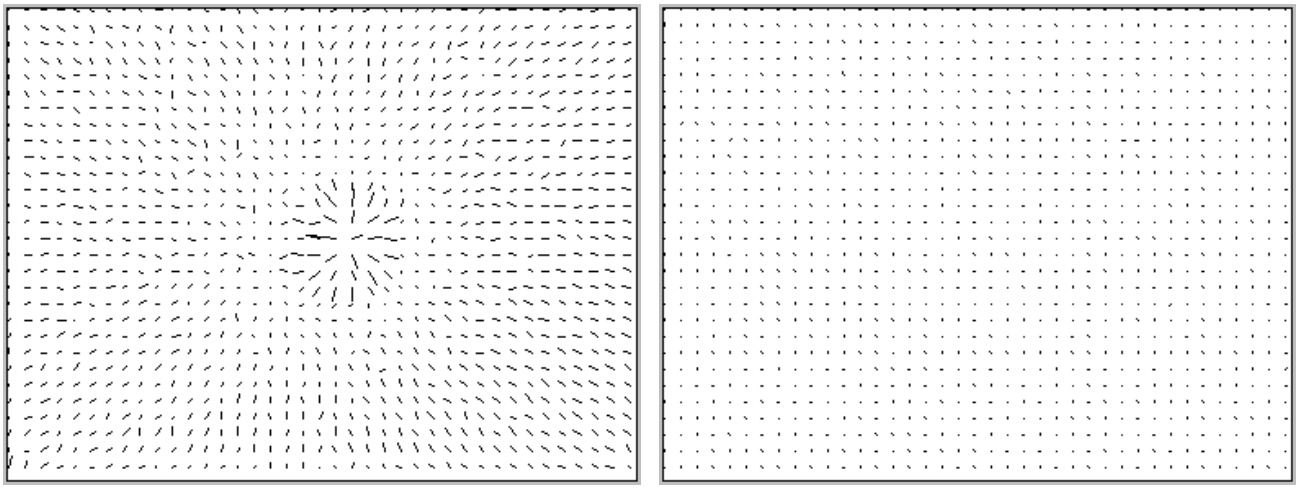

Figure 4 – Phase angle and amplitude of the brightness gradient in the recordings of Figure 3. Each vector marks the direction and amplitude of the brightness increase.

symmetric image. For the Mintron camera we would expect random phase angles. In reality, there are faint vertical and horizontal stripes in the original image which result from interferences and which show up markedly in the phase plot.

In case of the amplitude (Figure 6) we see the largest gradient of the image-intensified camera directly at the center, whereas the stripes in the Mintron recording are hardly visible. Some small rings are artifacts which result from the fact that bright stars cannot be removed completely by aperture photometry. At some point we simply have to define a threshold between a brightness increase caused by a strong gradient and by a nearby star.

After we solved the problem of the brightness gradient, we can now care about the variance estimation of star and meteor images (point spread function). We will see that there is no closed form solution this time, so that we have to estimate the variance iteratively by a robust method of approximation.

In the general case, a two-dimensional Gaussian (also called bi-variate normal distribution) of pixel values $h_{x,y}$ can be expressed by seven parameters:

- x- and y-coordinate of the center: μ_x and μ_y.
- Offset O (background brightness) and amplitude A (maximum brightness) of the normal distribution.
- Variances σ_x and σ_y of the normal distribution in x- and y-direction, and the correlation coefficient ρ between the two axes.

$$h_{x,y} = \frac{A}{2\pi\sigma_x\sigma_y\sqrt{1-\rho^2}} \times \\ \times \mathrm{e}^{\frac{-1}{2-2\rho^2}\left[\frac{(x-\mu_x)^2}{\sigma_x^2}+\frac{(y-\mu_y)^2}{\sigma_y^2}-\frac{2\rho(x-\mu_x)(y-\mu_y)}{\sigma_x\sigma_y}\right]} + O \quad (7)$$

An iterative approximation of seven free parameters would be extremely demanding, but luckily we can simplify the problem significantly:

- We assume a radial-symmetric Gaussian, i.e. $\sigma_x = \sigma_y = \sigma$ and $\rho = 0$.
- μ_x and μ_y are calculated as the mean x- and y-coordinates of all pixels belonging to the object,

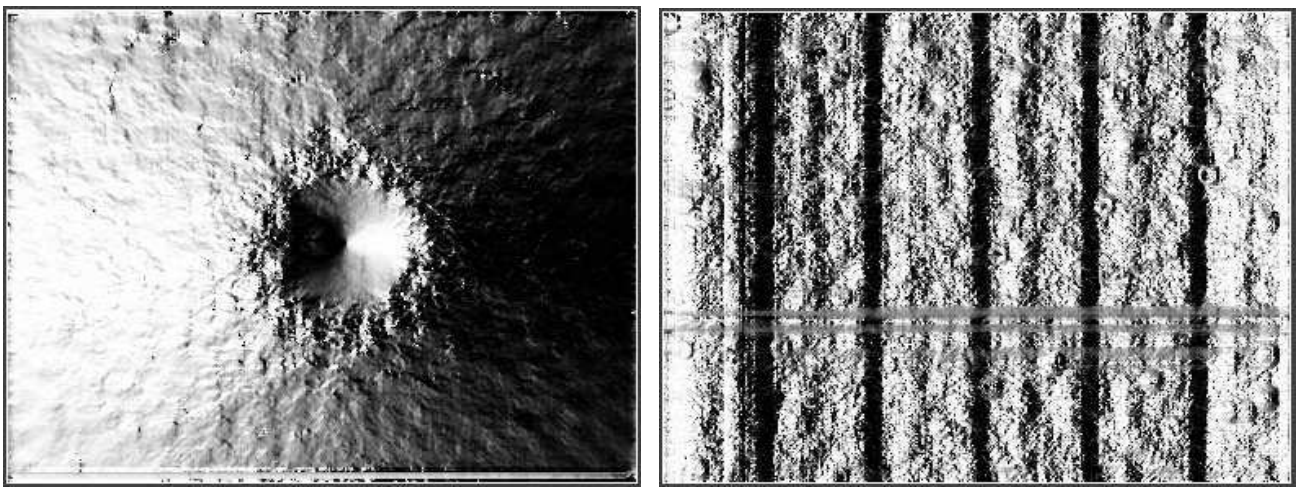

Figure 5 – Phase angle (coded in gray levels) of the brightness gradient for the recordings in Figure 3.

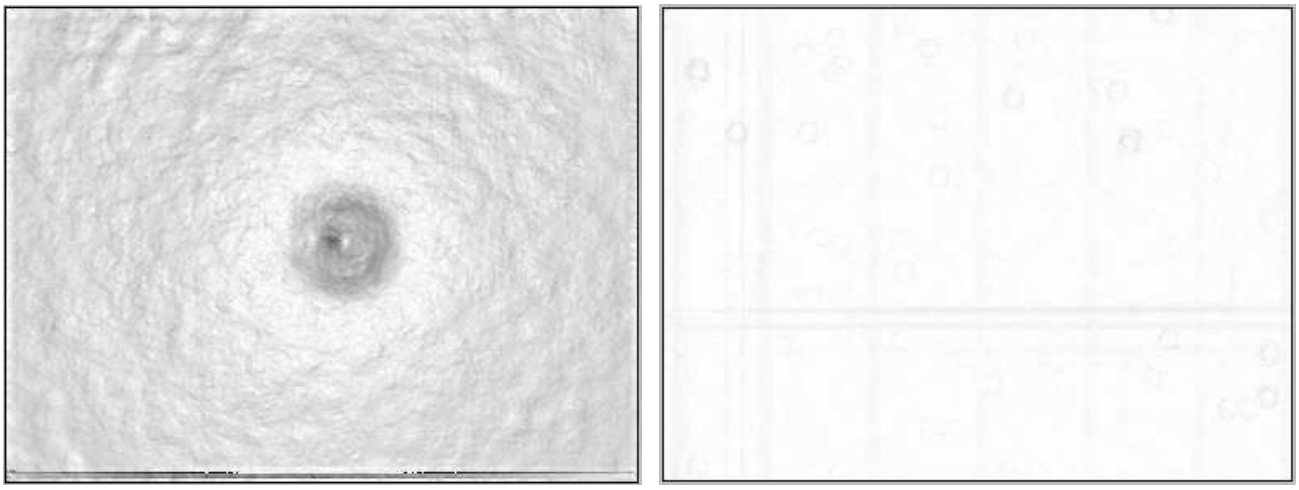

Figure 6 – Amplitude (coded in gray levels) of the brightness gradient for the recordings in Figure 3.

weighted by their brightness. At this step, the correction of the background brightness gradient described above is necessary to ensure that only pixels belonging to the object are included in the calculation.

- The background brightness O is determined by aperture photometry as described above.

Finally, we can remove the unknown amplitude A from the approximation scheme by summing up the pixel values cumulatively and normalizing the result in the end to unity.

In case of a radial-symmetric Gaussian, the x- and y-values are not relevant any more – only the distance d of the pixel from the center counts:

$$d = \sqrt{(x - \mu_x)^2 + (y - \mu_y)^2} \tag{8}$$

This way we can reduce the approximation method to a single free parameter, namely the variance σ^2:

- The distance d to the center is calculated for all pixels that belong to the object.
- The pixels are sorted by their distance from the center.
- The pixel values (reduced by the background) are accumulated with increasing d, and in the end the values are divided by the total pixel sum to obtain a normalized distribution.

$$V_d = \frac{\Sigma_0^d (h_d - O)}{\Sigma_0^\infty (h_d - O)} \tag{9}$$

The cumulative distribution V_d represents, what percentage of the overall brightness of an object is found up to distance d from the center. The distribution has a characteristic form that only depends on the variance σ^2. Objects with small variance will concentrate most of the light near the center, whereas in case of larger variance pixels farther away also contribute significantly to the overall brightness.

In order to determine the variance of a star, we first calculate the brightness distribution. Then we calculate iteratively the expected distribution V_d for different variances σ^2 and finally select the value with smallest difference between observed and expected distribution (least squares error).

For a one-dimensional normal distribution, the cumulative distribution corresponds to the Gaussian error function $\mathrm{erf}(x)$. For bi-variate normal distributions,

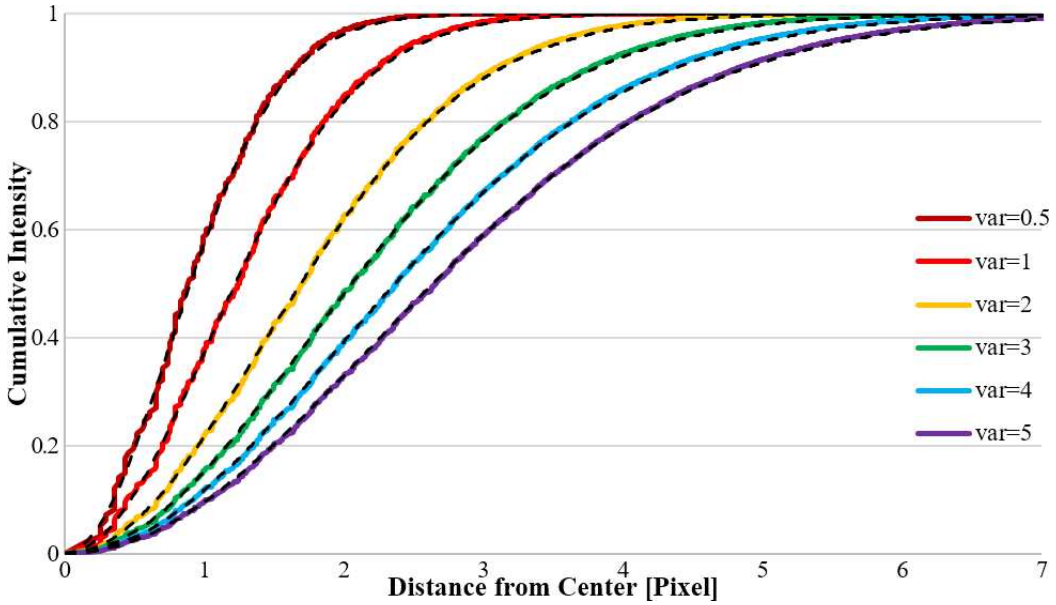

Figure 7 – Cumulative distribution function of a two-dimensional Gaussian calculated by computer simulation (solid colored lines) and the corresponding approximations by Equation 10 (dashed black lines).

however, there is no closed form solution for the distribution V_d. For this reason, we applied the same simulation that was used in March (Molau et al., 2016) to determine the limiting magnitude loss depending on the meteor angular velocity. The computer calculated for different variances σ^2 a high resolution two-dimensional Gaussian and simulated the mapping to a CCD chip of lower resolution. From the CCD image we obtained the cumulative distribution function V_d as described above, and then we searched empirically for an equation that would approximate the distribution function best. Not surprisingly, the error function $\mathrm{erf}(x)$ plays a central role in the resulting equation:

$$V_d = \mathrm{erf}\left(\frac{2d}{\pi\sqrt{\sigma^2 + 0.092}}\right)^2 \qquad (10)$$

Figure 7 shows the cumulative distributions V_d for different variances σ^2 obtained by the computer model, and the approximation by Equation 10 (black dashed lines). The correction term of 0.09 is already known from the March analysis. Also there we had to increase the variance by a constant factor of 0.09, because CCD pixels are not punctiform and have an integrative effect. Most likely the same explanation accounts for the offset here.

Now we still have to solve the practical problem, that in case of real video footage the stars consist typically of only a few pixels such that the cumulative distribution function relies on only a few support points. We could calculate the variance independently for each star because it may vary within the field of view (e.g. a larger variance near the edges caused by vignetting), but we want to work only with one variance value per camera. Ideally we should combine the measurements of all bright stars in the field of view into a single cumulative distribution to get a reliable estimate for the variance.

A simulation with different Gaussians having the same variance but different amplitude confirmed, that we may indeed combine different objects. For this purpose we do not calculate the distribution V_d for each star independently, but we combine all pixels from all stars. For each pixel we calculate the distance d to the center of the corresponding star, sort the pixels by increasing distance from the center, calculate the cumulative distribution over all pixels and normalize the distribution by dividing each value by the total pixel sum. For the resulting distribution we calculate the best-fitting variance by the approximation method described above.

So far for the theory. Which variances we obtain practically for different IMO Video Meteor Network cameras and what influence that has on the transformation from stellar to meteor limiting magnitude will be shown soon.

References

Molau S., Crivello S., Goncalves R., Saraiva C., Stomeo E., and Kac J. (2016). "Results of the IMO Video Meteor Network – March 2016, and discussion about the meteor limiting magnitude". *WGN, Journal of the IMO*, **44:4**, 120–126.

Handling Editor: Javor Kac

Code	Name	Location	Camera	FOV [°²]	Stellar LM [mag]	Eff.CA [km²]	Nights	Time [h]	Meteors
ARLRA	Arlt	Ludwigsfelde/DE	Ludwig2 (0.8/8)	1475	6.2	3779	26	89.3	431
BERER	Berkó	Ludányhalászi/HU	Hulud1 (0.8/3.8)	5542	4.8	3847	8	40.6	168
BOMMA	Bombardini	Faenza/IT	Mario (1.2/4.0)	5794	3.3	739	27	122.2	378
BREMA	Breukers	Hengelo/NL	Mbb3 (0.75/6)	2399	4.2	699	16	49.1	76
BRIBE	Klemt	Herne/DE	Hermine (0.8/6)	2374	4.2	678	18	57.6	117
		Bergisch Gladbach/DE	Klemoi (0.8/6)	2286	4.6	1080	19	48.3	96
CASFL	Castellani	Monte Baldo/IT	Bmh1 (0.8/6)	2350	5.0	1611	22	92.3	222
			Bmh2 (1.5/4.5)*	4243	3.0	371	20	74.4	131
CRIST	Crivello	Valbrevenna/IT	Bilbo (0.8/3.8)	5458	4.2	1772	25	108.3	318
			C3P8 (0.8/3.8)	5455	4.2	1586	22	91.2	232
			Stg38 (0.8/3.8)	5614	4.4	2007	24	109.6	541
DONJE	Donani	Faenza/IT	Jenni (1.2/4)	5886	3.9	1222	25	139.1	452
ELTMA	Eltri	Venezia/IT	Met38 (0.8/3.8)	5631	4.3	2151	18	79.7	163
FORKE	Förster	Carlsfeld/DE	Akm3 (0.75/6)	2375	5.1	2154	16	60.1	201
GONRU	Goncalves	Tomar/PT	Templar1 (0.8/6)	2179	5.3	1842	29	166.1	553
			Templar2 (0.8/6)	2080	5.0	1508	27	157.4	387
			Templar3 (0.8/8)	1438	4.3	571	26	143.5	129
			Templar4 (0.8/3.8)	4475	3.0	442	26	155.3	399
			Templar5 (0.75/6)	2312	5.0	2259	28	146.4	353
GOVMI	Govedič	Središče ob Dravi/SI	Orion2 (0.8/8)	1447	5.5	1841	24	101.5	218
			Orion3 (0.95/5)	2665	4.9	2069	27	95.6	147
			Orion4 (0.95/5)	2662	4.3	1043	25	87.6	148
HERCA	Hergenrother	Tucson/US	Salsa3 (0.8/3.8)	2336	4.1	544	24	166.4	276
IGAAN	Igaz	Budapest/HU	Hupol (1.2/4)	3790	3.3	475	14	67.5	35
JONKA	Jonas	Budapest/HU	Husor (0.95/4)	2286	3.9	445	21	96.3	114
			Husor2 (0.95/3.5)	2465	3.9	715	23	106.3	134
KACJA	Kac	Ljubljana/SI	Orion1 (0.8/8)	1399	3.8	268	19	78.3	216
		Kamnik/SI	Cvetka (0.8/3.8)*	4914	4.3	1842	15	74.5	293
			Rezika (0.8/6)	2270	4.4	840	15	77.8	400
			Stefka (0.8/3.8)	5471	2.8	379	12	66.1	148
KOSDE	Koschny	Izana Obs./ES	Icc7 (0.85/25)*	714	5.9	1464	23	164.5	1341
			Lic1 (2.8/50)*	2255	6.2	5670	30	231.3	2012
		La Palma/ES	Icc9 (0.85/25)*	683	6.7	2951	26	160.2	1574
			Lic2 (3.2/50)*	2199	6.5	7512	28	200.8	1730
LOJTO	Łojek	Grabniak/PL	Pav57 (1.0/5)	1631	3.5	269	18	79.7	199
LOPAL	Lopes	Lisbon/PT	Naso1 (0.75/6)	2377	3.8	506	20	115.7	59

Table 1 – Observers contributing to 2016 June data of the IMO Video Meteor Network. Eff.CA designates the effective collection area; the overall number of nights is the number of nights with at least one camera operating, the overall observing time and number of meteors are sums over all cameras.

Table 1 – Observers contributing to 2016 June data of the IMO Video Meteor Network – continued from previous page.

Code	Name	Location	Camera	FOV [°²]	Stellar LM [mag]	Eff.CA [km²]	Nights	Time [h]	Meteors
MACMA	Maciejewski	Chełm/PL	Pav35 (0.8/3.8)	5495	4.0	1584	27	103.3	346
			Pav36 (0.8/3.8)*	5668	4.0	1573	25	98.5	273
			Pav43 (0.75/4.5)*	3132	3.1	319	24	94.0	131
			Pav60 (0.75/4.5)	2250	3.1	281	22	89.0	273
MARGR	Maravelias	Lofoupoli-Crete/GR	Loomecon (0.8/12)	738	6.3	2698	10	36.3	40
MARRU	Marques	Lisbon/PT	Cab1 (0.8/3.8)	5291	3.1	467	27	179.7	364
			Ran1 (1.4/4.5)	4405	4.0	1241	27	148.4	244
MASMI	Maslov	Novosibirsk/RU	Nowatec (0.8/3.8)	5574	3.6	773	17	25.6	70
MOLSI	Molau	Seysdorf/DE	Avis2 (1.4/50)*	1230	6.9	6152	20	38.1	176
			Escimo2 (0.85/25)	155	8.1	3415	20	73.0	127
			Mincam1 (0.8/8)	1477	4.9	1084	17	55.9	159
		Ketzür/DE	Remo1 (0.8/8)	1467	6.5	5491	25	90.5	549
			Remo2 (0.8/8)	1478	6.4	4778	24	91.6	397
			Remo3 (0.8/8)	1420	5.6	1967	3	5.7	20
			Remo4 (0.8/8)	1478	6.5	5358	25	92.2	389
MORJO	Morvai	Fülöpszállás/HU	Huful (1.4/5)	2522	3.5	532	25	118.2	113
MOSFA	Moschini	Rovereto/IT	Rover (1.4/4.5)	3896	4.2	1292	17	10.4	48
OTTMI	Otte	Pearl City/US	Orie1 (1.4/5.7)	3837	3.8	460	27	128.6	194
PERZS	Perkó	Becsehely/HU	Hubec (0.8/3.8)*	5498	2.9	460	23	98.5	256
ROTEC	Rothenberg	Berlin/DE	Armefa (0.8/6)	2366	4.5	911	20	36.2	86
SARAN	Saraiva	Carnaxide/PT	Ro1 (0.75/6)	2362	3.7	381	23	101.8	145
			Ro2 (0.75/6)	2381	3.8	459	20	117.9	194
			Ro3 (0.8/12)	710	5.2	619	21	123.6	316
			Sofia (0.8/12)	738	5.3	907	18	92.1	103
SCALE	Scarpa	Alberoni/IT	Leo (1.2/4.5)*	4152	4.5	2052	20	85.8	74
SCHHA	Schremmer	Niederkrüchten/DE	Doraemon (0.8/3.8)	4900	3.0	409	17	42.5	83
SLAST	Slavec	Ljubljana/SI	Kayak1 (1.8/28)	563	6.2	1294	19	82.5	217
			Kayak2 (0.8/12)	741	5.5	920	17	73.3	116
STOEN	Stomeo	Scorze/IT	Min38 (0.8/3.8)	5566	4.8	3270	25	80.1	357
			Noa38 (0.8/3.8)	5609	4.2	1911	24	83.9	281
			Sco38 (0.8/3.8)	5598	4.8	3306	27	84.8	401
STRJO	Strunk	Herford/DE	Mincam2 (0.8/6)	2354	5.4	2751	18	55.8	172
			Mincam3 (0.8/6)	2338	5.5	3590	17	43.5	110
			Mincam4 (1.0/2.6)	9791	2.7	552	14	45.5	45
			Mincam5 (0.8/6)	2349	5.0	1896	17	45.6	56
			Mincam6 (0.8/6)	2395	5.1	2178	20	48.5	96
TEPIS	Tepliczky	Agostyán/HU	Huago (0.75/4.5)	2427	4.4	1036	21	103.8	115
			Humob (0.8/6)	2388	4.8	1607	25	106.4	238
TRIMI	Triglav	Velenje/SI	Sraka (0.8/6)*	2222	4.0	546	20	35.1	84
* active field of view smaller than video frame						Overall	30	6 966.8	21 849

Results of the IMO Video Meteor Network — July 2016

Sirko Molau[1], *Stefano Crivello*[2], *Rui Goncalves*[3], *Carlos Saraiva*[4], *Enrico Stomeo*[5], *and Javor Kac*[6]

A summary of the IMO Video Meteor Network in 2016 July is presented. Flux density profiles are presented for the α-Capricornids and Southern δ-Aquariids. The short outburst of the July γ-Draconids was well covered by the Network. The maximum occurred at $\lambda = 125.^{\circ}132$ (2016 July 28 at $00^{\mathrm{h}}07^{\mathrm{m}}$ UT) with a flux density of 23 meteoroids per 1000 km^2 per hour, equivalent to ZHR$\sim$ 100 using population index $r = 2.0$, as obtained from observations.

Received 2016 November 24

1 Introduction

July 2016 was an exceptional month as can be seen easily. Similar to the previous year, there are hardly any "holes" in the observing statistics, because the observing conditions were nearly perfect. In particular, in southern Europe, clouds in the night sky were the exception, such that five cameras in Italy and Portugal obtained 31 observing nights. 63 of 76 overall active cameras managed to observe in twenty or more observing nights. If we do not count those cameras which had to pause because of technical defects or other reasons, there was hardly any camera that did not take this hurdle because of the weather. Only in Slovenia, the weather conditions were not that good.

In total, we collected over 8 600 hours of effective observing time, which is about 10% less than in the previous year. This is because there were also eight cameras less than in July 2015. Since all four cameras on the Canary Islands run in high gear, we increased the overall number of meteors by 10% relative to 2015 to over 41 000 (Table 1 and Figure 1).

For the first time in a few months, a new camera dubbed Farelho1 joined the network, operated by Rui Goncalves. Responsibility for the Italian camera Bmh2 was taken over by Maurizio Carli.

2 July meteor showers

The most important meteor showers of July are the α-Capricornids and the Southern δ-Aquariids. Since both showers reach their peak at the end of the month, we included the already partially available August data in this analysis to get a complete activity profile for 2016.

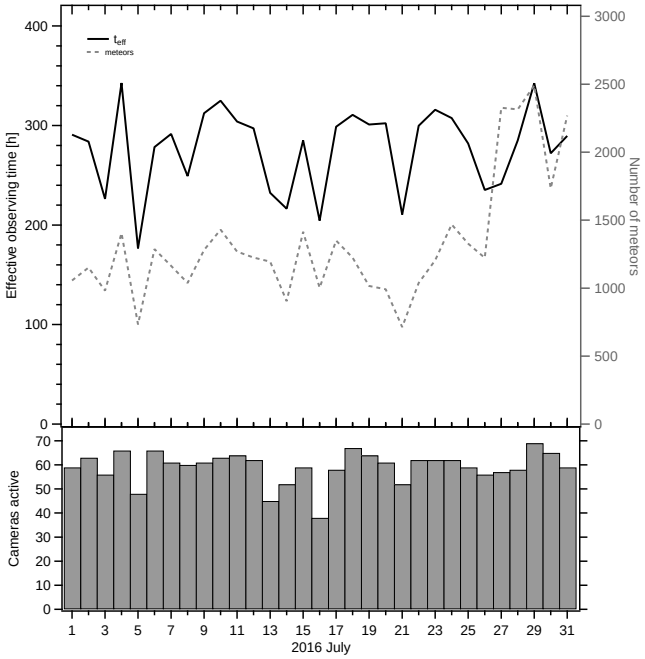

Figure 1 – Monthly summary for the effective observing time (solid black line), number of meteors (dashed gray line) and number of cameras active (bars) in 2016 July.

2.1 α-Capricornids

Figure 2 compares the overall activity profile of the α-Capricornids in 2015 and 2016. The peak rate in 2016 was clearly lower, since the peak flux density was only 2 meteoroids per 1 000 km^2 per hour, compared to 3 meteoroids per 1 000 km^2 per hour in the previous year. Earlier analyses had shown, though, that the flux density at full Moon is frequently estimated higher than at new Moon. The α-Capricornid peak of 2015 occurred directly at full Moon, whereas the peak of 2016 happened just before new Moon.

2.2 Southern δ-Aquariids

In case of the Southern δ-Aquariids (Figure 3) we can observe the same effect. Also here the 2015 peak flux density of almost 35 meteoroids per 1 000 km^2 per hour was higher than the peak flux density of 2016 which hardly exceeded 25 meteoroids per 1 000 km^2 per hour.

2.3 July γ-Draconids

In the end, however, it was another shower that made a splash in July. The July γ-Draconids sparked some

[1]Abenstalstr. 13b, 84072 Seysdorf, Germany. Email: sirko@molau.de
[2]Via Bobbio 9a/18, 16137 Genova, Italy. Email: stefano.crivello@libero.it
[3]Urbanizacao da Boavista, Lote 46, Linhaceira, 2305-114 Asseiceira, Tomar, Portugal. Email: rui.goncalves@ipt.pt
[4]Rua Aquilino Ribeiro, 23 - 1 Dto. 2790028 Carnaxide, Portugal. Email: carlos.saraiva@netcabo.pt
[5]via Umbria 21/d, 30037 Scorze (VE), Italy. Email: stom@iol.it
[6]Na Ajdov hrib 24, 2310 Slovenska Bistrica, Slovenia. Email: javor.kac@orion-drustvo.si

IMO bibcode WGN-446-molau-vidjul
NASA-ADS bibcode 2016JIMO...44..206M

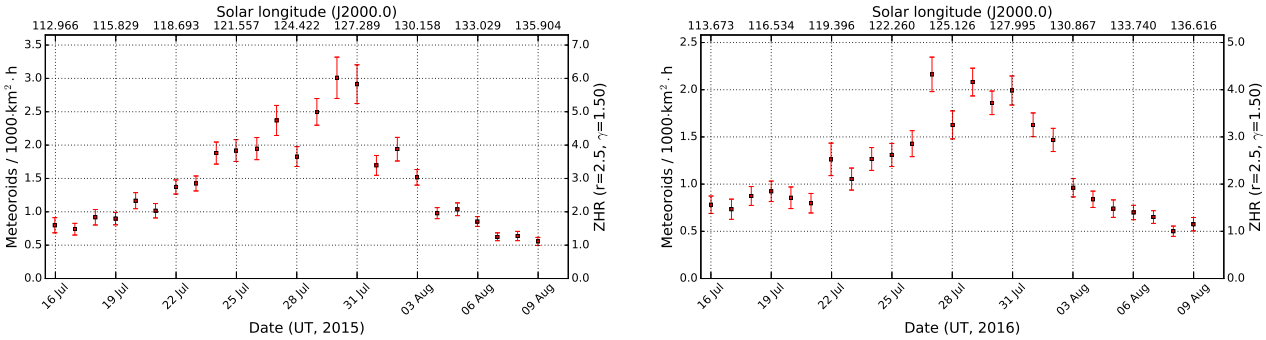

Figure 2 – Activity profile of the α-Capricornids in 2015 (left) and 2016 (right), derived from video observations of the IMO Video Meteor Network.

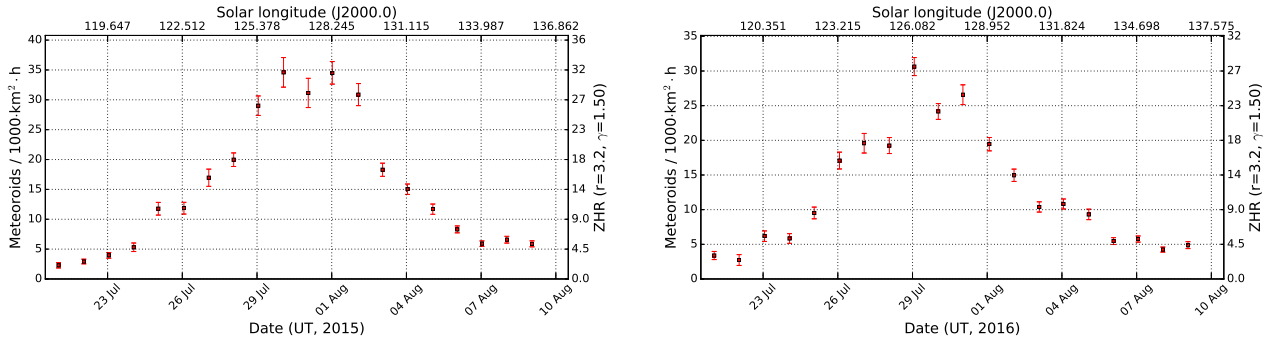

Figure 3 – Activity profile of the Southern δ-Aquariids in 2015 (left) and 2016 (right), derived from video observations of the IMO Video Meteor Network.

funny comments with their short code GDR over 25 years after the German reunification[a]. Indeed, they are a shower that was acquainted to only a few observers before. In our 2012 meteor shower analysis, we assigned about 700 meteors between 122° and 127° solar longitude to the July γ-Draconids, which are in principle easy to observe in northern latitudes thanks to their high declination and low velocity.

On July 30 Martin Breukers informed us that the CAMS Benelux network had recorded over 50 July γ-Draconids in less than two hours on July 27/28 close to midnight, among them five double-station meteors. Shortly thereafter we received a message from Peter Brown, that also the Canadian CMOR radar had captured an unexpected GDR outburst at midnight UT of July 27/28. The activity was 18 Sigma above the average and thus higher than the κ-Cancrid and γ-Lyrid outbursts that we had analysed in the February report (Molau et al., 2016).

Since there was obviously an unusual event, we asked the IMO Video Meteor Network observers to provide their observations on short notice. Thanks to this we could publish a first detailed activity profile of the July γ-Draconid outburst on the IMO homepage five days after the event. Based on a preliminary data set of 26 cameras we derived a peak flux density of 30 meteoroids per 1 000 km^2 per hour with a full width at half maximum (FWHM) of just one hour.

[a]the same abbreviation was used for the German Democratic Republic

Almost in parallel, Enrico Stomeo and Stefano Crivello informed about unusual activity end of July from the constellation of Draco which they had noted in the Italian camera data. Hence, they had discovered the outburst independently of the other observers, which makes the July γ-Draconids a perfect example for international data exchange and cooperation among meteor observers.

Now that the complete July data set of the IMO Video Meteor Network is available, we can refine the findings. In the two hours of the outburst we recorded over 500 July γ-Draconids, which allows us to obtain a high-resolution activity profile.

Figure 4 shows a comparison of the July γ-Draconid activity between 2011 and 2016. It is clear that the flux density of this year exceeded the average activity level many times.

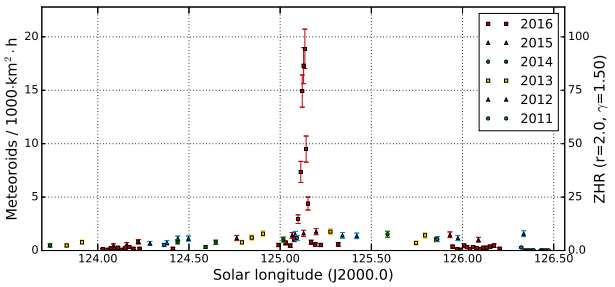

Figure 4 – Activity profile of the July γ-Draconids in the years 2011 to 2016, derived from video observations of the IMO Network.

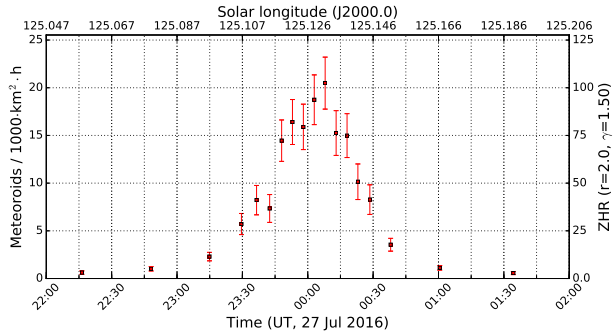

Figure 5 – Detailed activity profile of the July γ-Draconids on 2016 July 27/28, with a temporal resolution of five minutes per interval.

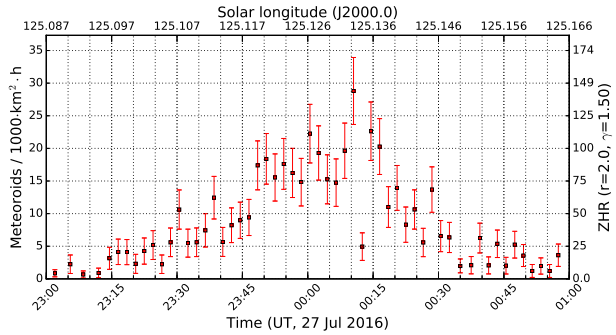

Figure 6 – Extremely high resolution activity profile of the July γ-Draconids on 2016 July 27/28, with a temporal resolution of just two minutes per interval.

At a resolution of five minutes per interval (Figure 5) we obtain a nice overall outburst profile. We can see that the activity raised only after 23^h UT on July 27 and had vanished before 01^h UT on July 28. Peak activity occurred briefly after midnight.

If the resolution is pushed to the limits (interval length two minutes) we find further interesting details (Figure 6).

First of all, we can precisely determine the peak time and FWHM of the outburst by fitting an exponential function to the ascending and descending activity branch. In the logarithmic presentation (Figure 7) those exponential functions show up as straight lines.

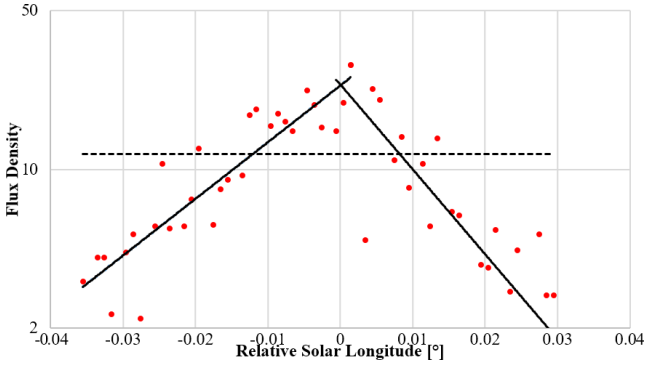

Figure 7 – Activity profile of the July γ-Draconids in logarithmic presentation. The solid black lines represent exponential fits to the ascending and descending activity branch, the horizontal dashed line is the half peak level.

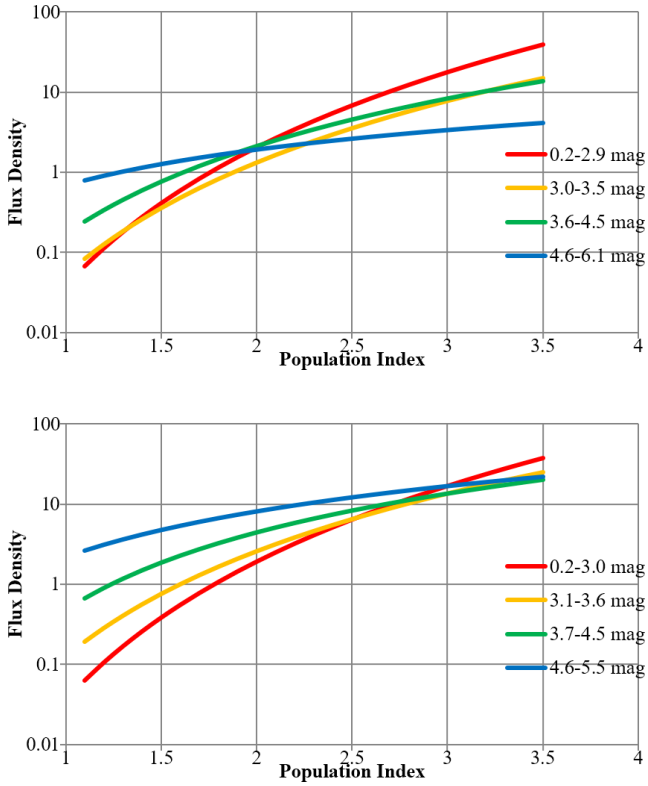

Figure 8 – Determination of the r-value of the July γ-Draconids (top) and sporadic meteors (bottom) on 2016 July 27/28.

We obtain a peak flux density of 23 meteoroids per 1 000 km^2 per hour at a solar longitude of 125 °.132 (2016 July 28, 00^h07^m UT). The times of half activity are 23^h49^m and 00^h19^m UT, which yields a FWHM of exactly 30 minutes. The descending branch was slightly steeper than the ascending branch.

The population index obtained by the usual method from video data of July 27/28 was $r = 2.0$ for the July γ-Draconids, and $r = 3.0$ for sporadic meteors, respectively. Thus, the population index was quite small and the percentage of bright shower meteors accordingly high.

With a population index of $r = 2.0$ we obtained an impressive equivalent ZHR of over 100 at the peak time (see Figure 6)! Compared to our initial analysis early August the flux density has become somewhat smaller, but the eZHR has clearly increased due to the smaller population index. The duration of the outburst was also only half as long as originally determined.

The high-resolution profile shows still another interesting detail. Scatter is naturally increasing at such short interval lengths, but immediately after the peak count at 00^h10^m UT (31 meteors, flux density 29) the rate breaks down by over 80% (5 meteors, flux density 5) only to be back at the original level in the next interval at 00^h14^m (25 meteors, flux density 23). This outlier was not used when the exponential fit was calculated, because it had distorted the fit significantly.

Now is that outlier just extended scatter or does it represent a real structure? If the meteor rate λ is constant and the individual meteors are mutually inde-

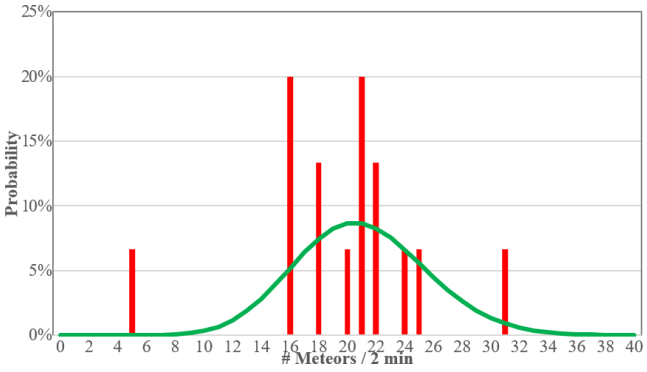

Figure 9 – Poisson distribution for an average of $\lambda = 21$ meteor per interval (green line) and really observed meteor counts per interval (red bars) during those 30 minutes of more than half peak activity.

pendent, the number of meteors k per time unit follows a Poisson distribution (Equation (1)):

$$P_\lambda(k) = \frac{\lambda^k}{k!}\mathrm{e}^{-\lambda} \qquad (1)$$

Between $23^\mathrm{h}49^\mathrm{m}$ and $00^\mathrm{h}19^\mathrm{m}$ we recorded on average of 21 July γ-Draconids per 2-min-interval. Figure 9 shows the probability that at an average activity of $\lambda = 21$ between $k = 0$ to 40 meteors are recorded per interval. It also shows how many meteors were observed in reality in these 15 intervals. We can see two outliers left and right. The probability that under the given conditions only five meteors are observed in a single interval is below one *per mille*. At large values of λ, the Poisson distribution resembles a normal distribution. From that we can estimate that the outlier was 4σ away from the average. The upper outlier is not unusual, though, in particular if we remember that it was observed at the peak time where the activity was rather like 25 meteors per interval.

We can sum up that the short time activity breakdown right after the peak is no statistical fluctuation but, with high probability, a real structure in the profile.

References

Molau S., Crivello S., Goncalves R., Saraiva C., Stomeo E., and Kac J. (2016). "Results of the IMO Video Meteor Network – March 2016, and discussion about the meteor limiting magnitude". *WGN, Journal of the IMO*, **44:4**, 120–126.

Handling Editor: Javor Kac

Code	Name	Location	Camera	FOV [°²]	Stellar LM [mag]	Eff.CA [km²]	Nights	Time [h]	Meteors
ARLRA	Arlt	Ludwigsfelde/DE	Ludwig2 (0.8/8)	1475	6.2	3779	26	85.5	598
BERER	Berkó	Ludányhalászi/HU	Hulud1 (0.8/3.8)	5542	4.8	3847	16	87.5	593
BOMMA	Bombardini	Faenza/IT	Mario (1.2/4.0)	5794	3.3	739	30	166.9	979
BREMA	Breukers	Hengelo/NL	Mbb3 (0.75/6)	2399	4.2	699	25	81.2	260
BRIBE	Klemt	Herne/DE	Hermine (0.8/6)	2374	4.2	678	26	74.8	285
		Bergisch Gladbach/DE	Klemoi (0.8/6)	2286	4.6	1080	27	75.1	237
CARMA	Carli	Monte Baldo/IT	Bmh2 (1.5/4.5)*	4243	3.0	371	24	113.7	346
CASFL	Castellani	Monte Baldo/IT	Bmh1 (0.8/6)	2350	5.0	1611	26	138.4	532
CRIST	Crivello	Valbrevenna/IT	Bilbo (0.8/3.8)	5458	4.2	1772	29	162.1	813
			C3P8 (0.8/3.8)	5455	4.2	1586	30	137.7	651
			Stg38 (0.8/3.8)	5614	4.4	2007	31	170.2	1428
DONJE	Donani	Faenza/IT	Jenni (1.2/4)	5886	3.9	1222	31	187.4	1315
ELTMA	Eltri	Venezia/IT	Met38 (0.8/3.8)	5631	4.3	2151	30	131.0	594
FORKE	Förster	Carlsfeld/DE	Akm3 (0.75/6)	2375	5.1	2154	18	62.4	301
GONRU	Goncalves	Foz do Arelho/PT	Farelho1 (1.0/2.6)	6328	2.8	469	1	5.3	39
		Tomar/PT	Templar1 (0.8/6)	2179	5.3	1842	31	199.8	1021
			Templar2 (0.8/6)	2080	5.0	1508	31	190.5	859
			Templar3 (0.8/8)	1438	4.3	571	28	172.6	325
			Templar4 (0.8/3.8)	4475	3.0	442	31	195.7	857
			Templar5 (0.75/6)	2312	5.0	2259	30	174.6	824
GOVMI	Govedič	Središče ob Dravi/SI	Orion2 (0.8/8)	1447	5.5	1841	25	107.7	347
			Orion3 (0.95/5)	2665	4.9	2069	16	57.0	115
			Orion4 (0.95/5)	2662	4.3	1043	26	107.5	242
HERCA	Hergenrother	Tucson/US	Salsa3 (0.8/3.8)	2336	4.1	544	27	163.8	447
IGAAN	Igaz	Budapest/HU	Hupol (1.2/4)	3790	3.3	475	23	108.1	136
JONKA	Jonas	Budapest/HU	Husor (0.95/4)	2286	3.9	445	25	121.9	244
			Husor2 (0.95/3.5)	2465	3.9	715	25	117.0	255
KACJA	Kac	Ljubljana/SI	Orion1 (0.8/8)	1399	3.8	268	24	105.3	536
		Kamnik/SI	Cvetka (0.8/3.8)*	4914	4.3	1842	16	75.9	436
			Rezika (0.8/6)	2270	4.4	840	15	74.3	535
			Stefka (0.8/3.8)	5471	2.8	379	15	69.6	272
KOSDE	Koschny	Izana Obs./ES	Icc7 (0.85/25)*	714	5.9	1464	26	158.7	1274
			Lic1 (2.8/50)*	2255	6.2	5670	29	229.2	2688
		La Palma/ES	Icc9 (0.85/25)*	683	6.7	2951	21	145.9	1838
			Lic2 (3.2/50)*	2199	6.5	7512	30	233.8	2892
LOJTO	Łojek	Grabniak/PL	Pav57 (1.0/5)	1631	3.5	269	15	61.2	313
LOPAL	Lopes	Lisbon/PT	Naso1 (0.75/6)	2377	3.8	506	26	165.1	167

Table 1 – Observers contributing to 2016 July data of the IMO Video Meteor Network. Eff.CA designates the effective collection area; the overall number of nights is the number of nights with at least one camera operating, the overall observing time and number of meteors are sums over all cameras.

Table 1 – Observers contributing to 2016 July data of the IMO Video Meteor Network – continued from previous page.

Code	Name	Location	Camera	FOV [°²]	Stellar LM [mag]	Eff.CA [km²]	Nights	Time [h]	Meteors
MACMA	Maciejewski	Chełm/PL	Pav35 (0.8/3.8)	5495	4.0	1584	26	96.8	512
			Pav36 (0.8/3.8)*	5668	4.0	1573	28	95.9	389
			Pav43 (0.75/4.5)*	3132	3.1	319	25	64.9	250
			Pav60 (0.75/4.5)	2250	3.1	281	28	96.7	464
MARGR	Maravelias	Lofoupoli-Crete/GR	Loomecon (0.8/12)	738	6.3	2698	10	36.3	40
MARRU	Marques	Lisbon/PT	Cab1 (0.8/3.8)	5291	3.1	467	30	204.3	941
			Ran1 (1.4/4.5)	4405	4.0	1241	27	178.0	524
MASMI	Maslov	Novosibirsk/RU	Nowatec (0.8/3.8)	5574	3.6	773	22	47.4	179
MOLSI	Molau	Seysdorf/DE	Avis2 (1.4/50)*	1230	6.9	6152	24	87.4	888
			Escimo2 (0.85/25)	155	8.1	3415	23	114.2	326
			Mincam1 (0.8/8)	1477	4.9	1084	25	81.2	370
		Ketzür/DE	Remo1 (0.8/8)	1467	6.5	5491	27	96.7	823
			Remo2 (0.8/8)	1478	6.4	4778	28	96.9	645
			Remo3 (0.8/8)	1420	5.6	1967	1	5.0	32
			Remo4 (0.8/8)	1478	6.5	5358	27	99.7	687
MORJO	Morvai	Fülöpszállás/HU	Huful (1.4/5)	2522	3.5	532	29	146.1	267
MOSFA	Moschini	Rovereto/IT	Rover (1.4/4.5)	3896	4.2	1292	23	14.1	97
OTTMI	Otte	Pearl City/US	Orie1 (1.4/5.7)	3837	3.8	460	28	138.8	376
PERZS	Perkó	Becsehely/HU	Hubec (0.8/3.8)*	5498	2.9	460	20	102.3	474
ROTEC	Rothenberg	Berlin/DE	Armefa (0.8/6)	2366	4.5	911	23	46.1	134
SARAN	Saraiva	Carnaxide/PT	Ro1 (0.75/6)	2362	3.7	381	28	181.7	347
			Ro2 (0.75/6)	2381	3.8	459	27	186.4	500
			Ro3 (0.8/12)	710	5.2	619	26	170.3	682
			Sofia (0.8/12)	738	5.3	907	27	161.5	315
SCALE	Scarpa	Alberoni/IT	Leo (1.2/4.5)*	4152	4.5	2052	28	132.0	246
SCHHA	Schremmer	Niederkrüchten/DE	Doraemon (0.8/3.8)	4900	3.0	409	24	79.6	270
SLAST	Slavec	Ljubljana/SI	Kayak1 (1.8/28)	563	6.2	1294	17	67.3	332
			Kayak2 (0.8/12)	741	5.5	920	27	132.9	169
STOEN	Stomeo	Scorze/IT	Min38 (0.8/3.8)	5566	4.8	3270	30	145.4	987
			Noa38 (0.8/3.8)	5609	4.2	1911	30	149.4	836
			Sco38 (0.8/3.8)	5598	4.8	3306	30	144.6	1064
STRJO	Strunk	Herford/DE	Mincam2 (0.8/6)	2354	5.4	2751	28	82.0	325
			Mincam3 (0.8/6)	2338	5.5	3590	26	67.3	244
			Mincam4 (1.0/2.6)	9791	2.7	552	21	62.2	66
			Mincam5 (0.8/6)	2349	5.0	1896	22	67.8	143
			Mincam6 (0.8/6)	2395	5.1	2178	27	64.4	211
TEPIS	Tepliczky	Agostyán/HU	Huago (0.75/4.5)	2427	4.4	1036	25	120.9	270
			Humob (0.8/6)	2388	4.8	1607	3	13.9	110
TRIMI	Triglav	Velenje/SI	Sraka (0.8/6)*	2222	4.0	546	17	49.9	114
YRJIL	Yrjölä	Kuusankoski/FI	Finexcam (0.8/6)	2337	5.5	3574	2	3.9	24
* active field of view smaller than video frame						Overall	31	8 610.3	41 227

The International Meteor Organization

www.imo.net

Follow us on Facebook
InternationalMeteorOrganization

Follow us on Twitter
@IMOMeteors

Council

President: Cis Verbeeck,
Bogaertsheide 5, 2560 Kessel, Belgium.
e-mail: cis.verbeeck@scarlet.be

Vice-President: Jürgen Rendtel,
Eschenweg 16, D-14476 Marquardt, Germany.
tel. +49 33208 50753
e-mail: jrendtel@aip.de

Secretary-General: Robert Lunsford,
1828 Cobblecreek Street, Chula Vista,
CA 91913-3917, USA. tel. +1 619 585 9642
e-mail: lunro.imo.usa@cox.net

Treasurer: Marc Gyssens, Heerbaan 74,
B-2530 Boechout, Belgium.
e-mail: marc.gyssens@uhasselt.be
BIC: GEBABEBB
IBAN: BE30 0014 7327 5911
Bank transfer costs are always at your expense.

Other Council members:

Megan Argo, Jodrell Bank Centre for Astrophysics,
Alan Turing building, University of Manchester,
Oxford Road, Manchester, M13 9PL, UK.
e-mail: megan.argo@gmail.com

Geert Barentsen, NASA Ames Research Center,
M/S 244-30, Moffett Field CA 94035, USA.
e-mail: hello@geert.io

Javor Kac (see details under WGN)

Detlef Koschny, Zeestraat 46,
NL-2211 XH Noordwijkerhout, Netherlands.
e-mail: detlef.koschny@esa.int

Masahiro Koseki, 4-3-5 Annaka, Annaka-shi,
Gunma-ken 379-0116, Japan.
e-mail: geh04301@nifty.ne.jp

Sirko Molau, Abenstalstraße 13b, D-84072 Seysdorf,
Germany. e-mail: sirko@molau.de

Jean-Louis Rault, Société Astronomique de France,
16, rue de la Vallée, 91360 Epinay sur Orge,
France. e-mail: f6agr@orange.fr

Paul Roggemans, Pijnboomstraat 25, 2800 Mechelen,
Belgium, e-mail: paul.roggemans@gmail.com

Galina Ryabova, Res. Inst. of Appl. Math. & Mech.,
Tomsk State University, Lenin pr. 36, build. 27,
634050 Tomsk, Russian Federation.
e-mail: ryabova@niipmm.tsu.ru

Damir Šegon, J. Rakovca 3, 52100 Pula,
Croatia. e-mail: damir.segon@pu.t-com.hr

Juraj Tóth, Fac. Math., Phys. & Inf., Comenius
Univ., Mlynska dolina, 84248 Bratislava, Slovakia.
e-mail: toth@fmph.uniba.sk

Commission Directors

Visual Commission: Rainer Arlt (rarlt@aip.de)
Generic e-mail address: visual@imo.net
Electronic visual report form:
http://www.imo.net/visual/report/electronic

Video Commission: Sirko Molau (video@imo.net)

Photographic Commission: Bill Ward
(William.Ward@glasgow.ac.uk)
Generic e-mail address: photo@imo.net

Radio Commission: Jean-Louis Rault (radio@imo.net)

Fireballs: Online fireball reports:
http://fireballs.imo.net

Outreach Officer

Jure Atanackov, e-mail: jureatanackov@gmail.com

Press Officer

Megan Argo, e-mail: megan.argo@gmail.com

Webmaster

Karl Antier, e-mail: webmaster@imo.net

WGN

Editor-in-chief: Javor Kac
Na Ajdov hrib 24, SI-2310 Slovenska Bistrica,
Slovenia. e-mail: wgn@imo.net;
include METEOR in the e-mail subject line

Editorial board: Ž. Andreić, M. Argo, D.J. Asher,
F. Bettonvil, J. Correira, M. Gyssens,
C. Hergenrother, T. Heywood, J. Rendtel,
J.-L. Rault, C. Verbeeck, D. Vida, S. de Vet.

IMO Sales

Available from the Treasurer or the Electronic Shop on the IMO Website	€	$
IMO membership, including subscription to WGN Vol. 44 (2016)		
Surface mail	26	35
Air Mail (outside Europe only)	49	65
Electronic subscription only	21	25
Proceedings of the International Meteor Conference on paper		
1990, 1991, 1993, 1995, 1996, 1999, 2000, 2002, 2003, per year	9	12
2007, 2010, 2011, per year	15	20
2012, 2013, 2014, 2015 per year	25	34
2016	30	40
Proceedings of the Meteor Orbit Determination Workshop 2006	15	20
Radio Meteor School Proceedings 2005	15	20
Handbook for Meteor Observers	15	20
Meteor Shower Workbook	12	16
Electronic media		
Meteor Beliefs Project ZIP archive	6	8

Perseids on 2016 August 12/13 from Emberger Alm, Austria